ACS NANO
www.acsnano.org

Upcycling Spent Cathodes from Li−Ion Batteries into a High-Entropy Alloy Catalyst with Reverse Electron Transfer for Li−O_2 Batteries

Peng Wang,* Shan Guo, Yongbin Xu, Xinyi Yuan, Yu Tian, Binchao Xu, Zhijun Zhao, Yuxiao Wang, Jianwei Li, Xiaojun Wang, and Zhiming Liu*

Cite This: https://doi.org/10.1021/acsnano.5c00704

Read Online

ACCESS | Metrics & More | Article Recommendations | Supporting Information

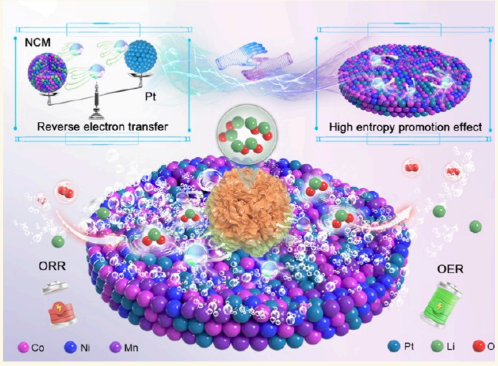

ABSTRACT: **Traditional recovery of valuable metals from spent ternary lithium-ion batteries concentrates on complicated pyrometallurgy and hydrometallurgy routes. Direct reutilization of these valuable used metals to catalyze Li−O_2 batteries is highly appealing yet remains a significant challenge. Here, we report a general synthesis of ultrafine αNiCoMn (α = Pt, Ir, Ru) high-entropy alloy (HEA) nanoparticles anchored on a nitrogen-doped carbon (N−C) support through a facile one-step Joule heating, which serves as a high-efficiency catalyst for Li−O_2 batteries. Solution alloying of recycled NiCoMn with Pt group metals facilitates catalytic efficiency through 3d−5d electronic interactions and the high-entropy assembly effect. Both experimental and calculation results reveal that, driven by rapid, non-equilibrium thermal shock, electron transfer defies conventional expectations, where the electrons are inclined to transfer from the higher electronegative Pt to the surrounding NiCoMn atoms. This interesting reverse local charge redistribution and orbital hybridization endow Pt with an elevated *d*-band center and an optimized electronic structure. The induced high-entropy coordination effects further generate highly active catalysis surfaces, favoring the adsorption of LiO_2 intermediates and facilitating rapid decomposition kinetics of nanoscale Li_2O_2 products. These advantages endow Pt HEA@N−C with superior bifunctional catalytic activity, achieving an ultralow polarization of 0.27 V and a significantly enhanced cycling life of 240 cycles. We anticipate that this work will provide further insights into upcycling spent valuable metals for constructing efficient HEA electrocatalysts.**

KEYWORDS: *Li−O_2 batteries, high entropy, Li_2O_2, ORR/OER, kinetics*

INTRODUCTION

Nonproton lithium−oxygen (Li−O_2) batteries, with an unparalleled theoretical gravimetric energy density (3500 Wh kg^{-1}), are at the forefront of research to meet the urgent need for long-term operation of large energy storage devices. However, rechargeable Li−O_2 batteries face limitations such as diminished charge and discharge capacities, suboptimal rate performance, and a shortened life cycle. These challenges stem from the electrically insulating and insoluble characteristics of the discharge byproduct, lithium peroxide (Li_2O_2), which results in sluggish oxygen reduction reaction (ORR) and oxygen evolution reaction (OER) kinetics.[1−3] Addressing this challenging problem, numerous studies have concentrated on the rational design of various catalysts, aiming to improve the nucleation/growth/decomposition kinetics of Li_2O_2 during repeated redox processes, thereby optimizing the electrochemical performance of Li−O_2 batteries.[4−8]

In recent years, Pt group noble metal catalysts have been regarded as state-of-the-art electrocatalysts for Li−O_2 batteries due to their exceptional charge transfer rates and tunable electronic configurations.[9−13] Unfortunately, the scarcity and instability during cycling of Pt-based catalysts substantially impede their swift advancement in Li−O_2 battery technology. In

Received: January 12, 2025
Revised: April 17, 2025
Accepted: April 21, 2025

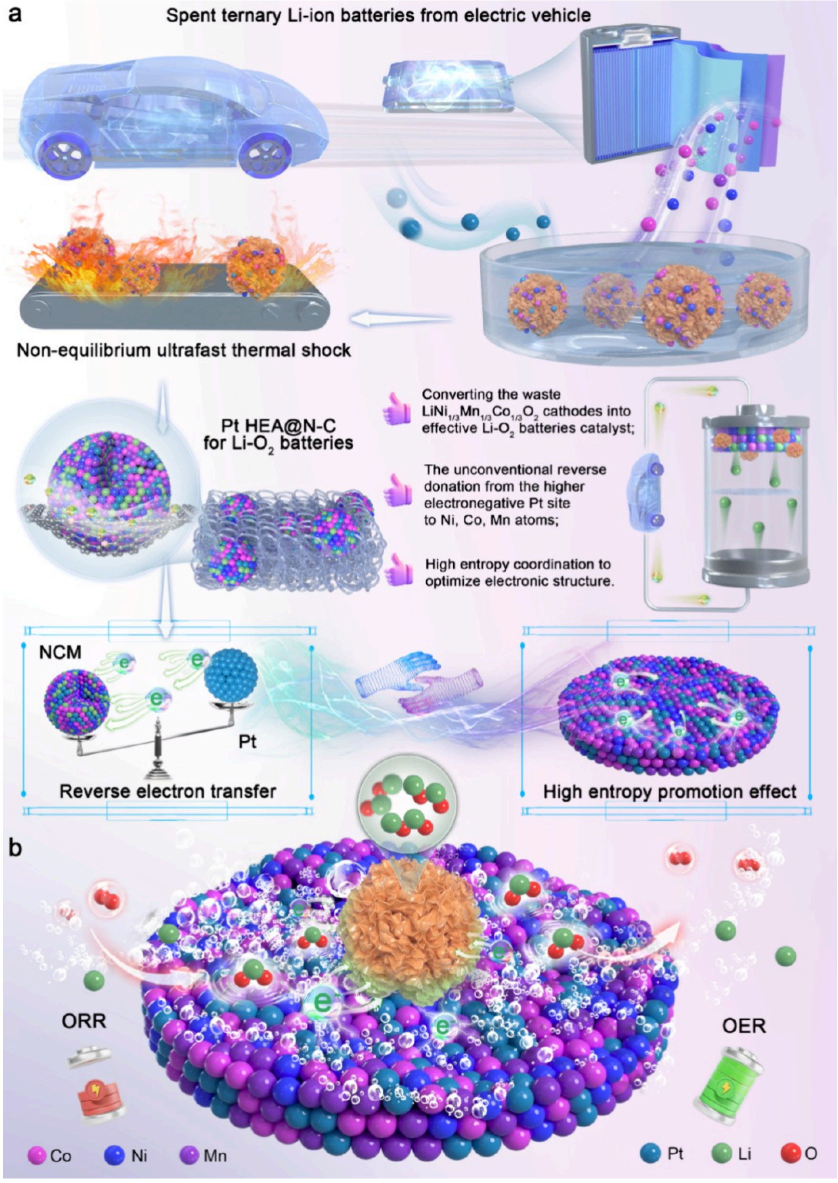

Figure 1. (a) Schematic illustration of the fabrication procedures and (b) underlying mechanism of the Pt HEA@N−C catalyst.

response, solid solution alloying with economical 3d transition metals (M) in a single phase can not only reduce cost but also realize electronic structure modulation. Thereinto, the 5d orbitals of Pt group atoms possess a large spatial extent of the d-electron wave function. Therefore, the synergistic conjunction of 3d−5d orbitals facilitates a reorganization of electron placement on the Pt group atoms' surface, resulting in electron delocalization. However, due to the larger electronegativity of Pt group atoms, electrons are inclined to transfer from the surrounding 3d transition metals to Pt group atoms during the alloying process, making the latter an electron-rich state.[14−17] Unfortunately, referring to Hammer and Norskov's d-band model, the higher occupancy in the e_g orbital of the Pt atom leads to a downshift of its *d*-band center toward the Fermi level, resulting from the increased filling of antibonding states. This effect further contributes to weakening the bonding with O 2p near the Fermi level and inhibiting the adsorption capability toward the oxygen-containing products/intermediates. For instance, Guo et al. reported that due to the reduced e_g electrons of Pt in PtAu compared with that in PtRu, the former catalyst demonstrates a stronger affinity for LiO_2 intermediates and thus enhanced OER kinetics.[18] It can be mentioned that these changes, in turn, are just not conducive to the electrochemistry performance improvement of the 3d−5d hybrid PtM catalyst for unique Li−O_2 batteries. Therefore, overcoming the conventional electronegativity-dominated electron donation/acceptance direction within PtM is critically important for its high-efficiency application in Li−O_2 batteries, yet it remains a big challenge.

Furthermore, in the PtM solid solution alloy catalyst, the ligand effects resulting from the synergistic interaction between different elements and the specific local coordination environment they form play a crucial role in the final catalytic activity. Therein, high-entropy alloys (HEAs), composed of 4−5 or more metal constituents with a similar molar ratio, have attracted much attention owing to their particular coordination and electron structure stemming from the multielement synergy, lattice strain, and cocktail effects.[19−24] These adjustable characteristics facilitate a sustainable catalytic activity origin for Li−O_2 batteries involving multiple intermediates. Interest-

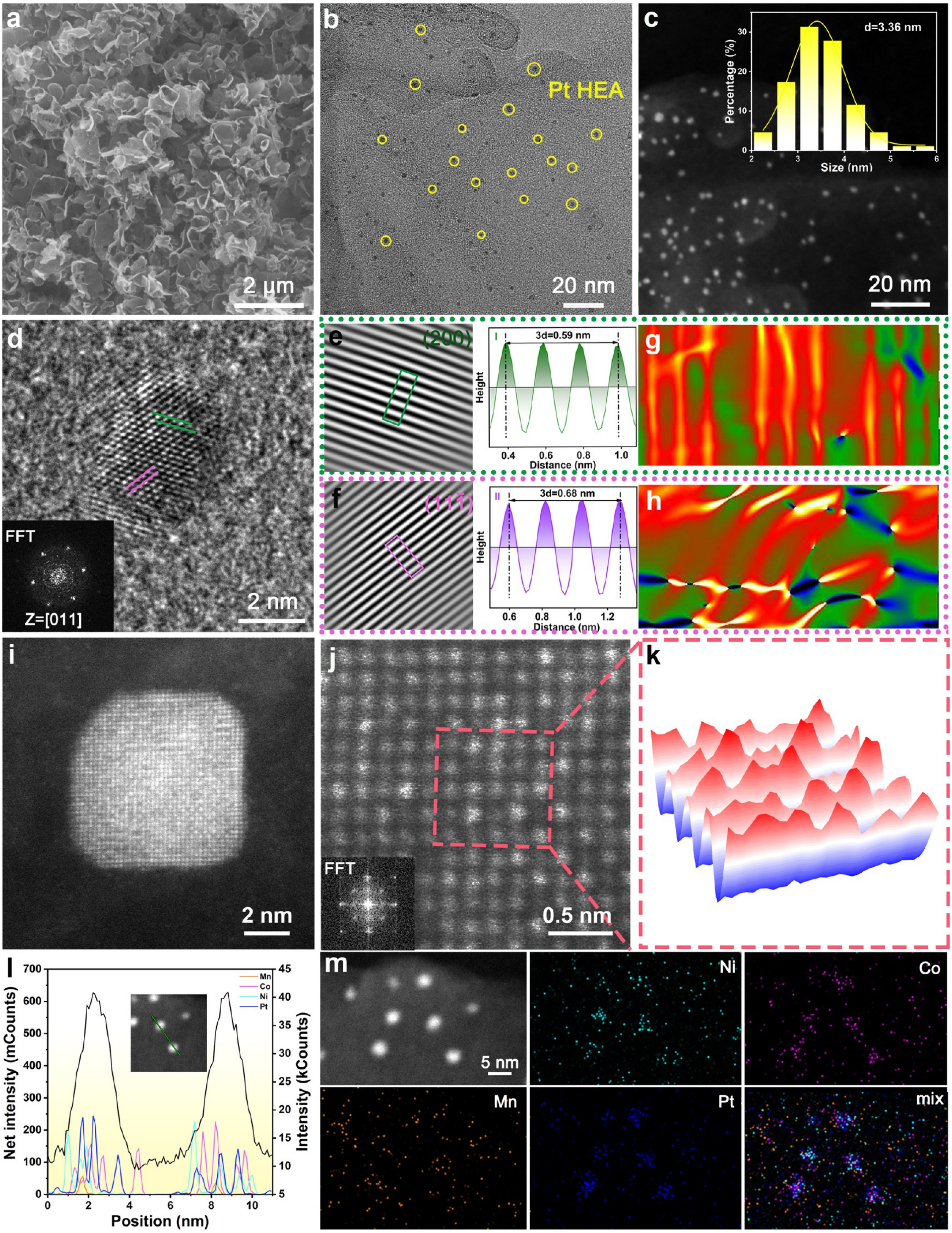

Figure 2. Morphology characterizations of Pt HEA@N−C. (a) SEM image, (b) TEM image, (c) HAADF-STEM image (inset, particle size distribution), and (d) HRTEM image (inset, FFT of the Pt HEA nanoparticle) of Pt HEA@N−C. (e) IFFT image and crystallite gaps diagram of the (200) plane and (f) IFFT image and crystallite gaps diagram of the (11$\bar{1}$) plane of the Pt HEA nanoparticle. (g) GPA of the (200) plane and

Figure 2. continued

(h) GPA of (the 11$\bar{1}$) plane of the Pt HEA nanoparticle. (i) HAADF-STEM image, (j) HAADF-STEM image (inset, FFT of the Pt HEA nanoparticle), and (k) 3D intensity distributions of Pt HEA@N−C. (l) Line scanning and (m) corresponding element mapping images of Pt HEA@N−C.

ingly, plenty of Ni, Co, and Mn valuable metals with unfilled valence d orbitals survive in the used $LiNi_{1-x-y}Mn_xCo_yO_2$ cathodes in lithium-ion batteries, which are ideal transition-metal sources for constructing PtM HEA. Recycling these valuable metals can mitigate public environmental threats and facilitate the circular use of metal resources, especially considering the considerable activity of Ni, Co, and Mn metals. However, the process of directly upcycling these high-value metals from spent ternary lithium-ion batteries to $Li-O_2$ batteries is still in its infancy.

In the present work, we demonstrate an example of the general synthesis of ultrafine αNiCoMn (α = Pt, Ir, Ru) HEA nanoparticles confined on a nitrogen-doped carbon (N−C) support through extracting Ni, Co, and Mn valuable metals from waste $LiNi_{1/3}Mn_{1/3}Co_{1/3}O_2$ cathodes. Especially, the high-energy transient shock from Joule heating contributes to thermodynamically driving the unconventional reverse donation of excess electron density from the higher electronegative Pt to neighboring Ni, Co, and Mn atoms with a smaller electronegativity, making them well-suited as high-efficiency catalysts for $Li-O_2$ batteries. It is experimentally and theoretically confirmed that the electronic structure and local coordination of Pt catalytic centers in Pt HEA@N−C are fundamentally activated by the electron donor of Ni, Co, and Mn. This special 3d−5d orbital hybridization leads to a positive shift in the *d*-band center of Pt, significantly boosting its adsorption energy toward oxygen-involved intermediates and efficiently regulating the morphology and distribution of the ultrathin petal-like Li_2O_2 during ORR. During the subsequent OER, this Li_2O_2 exhibits excellent decomposition efficiency and reversibility at the three-phase contact interfaces. This endows Pt HEA@N−C with the much-reduced energy barrier during both ORR and OER, resulting in an ultrasmall overall polarization of 0.27 V at 200 mA g^{-1} and a superior cycling performance exceeding 240 cycles at 400 mA g^{-1}. As a proof-of-concept, this work not only broadens the scope for the reuse of waste $LiNi_{1-x-y}Mn_xCo_yO_2$ cathodes to construct high-performance catalysts but also provides further insights into the *d*-band structure modulation of Pt group metals for versatile catalysis.

RESULTS AND DISCUSSION

Microstructural Characterization. Figure 1 schematically illustrates the controllable experimental preparation of Pt HEA@N−C. In detail, an end-of-life $LiNi_{1/3}Mn_{1/3}Co_{1/3}O_2$ ternary lithium-ion battery pack (nominal voltage of 3.6 V, nominal capacity of 100 Ah, open-circuit voltage of 3.97 V) from electric vehicles is first discharged to 1.0 V for residual energy release by a series of self-made parallel resistors (Figure S1). It is mentioned that this proposed mild physical discharge strategy is much safer, cost-effective, and environmentally friendly compared with the commonly reported NaCl solution immersion and acupuncture-induced short-circuit discharge methods. Then, after successive manual battery disassembly and acid leaching, mixed ionic solutions with Ni, Co, and Mn in a similar molar ratio are obtained (see Methods and Table S1). It is mentioned that according to the inductively coupled plasma optical emission spectrometry results, the concentrations of Ni, Co, and Mn in the recovered precursor solution were found to be about 1135.76, 1155.50, and 1140.88 mg L^{-1}, respectively, with a mole ratio close to 1:1:1. Subsequently, the as-obtained porous N−C ultrathin nanosheets are added into the homogeneously mixed Ni, Co, Mn, and Pt precursor solution for sufficient electrostatic adsorption. Afterward, the Pt HEA@N−C composite can be successfully prepared after being subjected to a rapid Joule heating procedure featuring a second-level heating−quenching. In this regard, Ni, Co, Mn, and Pt with diverse atomic radii and reduction potentials can be chemically bonded and thermally coreduced into Pt HEA in situ anchored on the skeleton of the N−C support. The highly disordered distribution of Ni, Co, and Mn atoms surrounding Pt atoms with near-equimolar proportions benefits the optimization of the electronic structure and maximizes the intrinsic catalytic kinetics of the activated Pt centers. More importantly, driven by the instantaneous shock in an extreme environment, an abnormal reverse donation of extra electron density from the higher electronegative Pt (2.28) to the neighboring lower electronegative Ni (1.91), Co (1.88), and Mn (1.55) atoms occurs, further regulating the adsorption characteristics toward intermediate products and resulting in favorable catalytic sites for $Li-O_2$ batteries. From this viewpoint, our strategy is based on the integration of direct NiCoMn ion separation from waste batteries, followed by rapid Joule heating. Meanwhile, it has greater advantages in terms of efficiency, the environment, and the economy and is committed to being an important alternative to the traditional complex pyrometallurgical and hydrometallurgical routes. In addition, the Pt@N−C and NCM@N−C counterparts, with the absence of recovered transition-metal and Pt sources, respectively, are also fabricated for comparison.

The morphological characteristics of the Pt HEA@N−C, Pt@N−C, and NCM@N−C composites were characterized. The scanning electron microscopy (SEM) images (Figures 2a, S2−S4) indicate that the porous carbon nanosheet skeleton is still well-inherited after incorporating abundant metal nanoparticles. Meanwhile, this curled nanosheet morphology facilitates an optimal microenvironment for liquid electrolyte permeation, mass-charge transport, and Li_2O_2 deposition. Notably, Pt HEA particles are not visible on the substrate surface in Figure 2a due to their ultrasmall size. Both bright-field transmission electron microscopy (TEM) image (Figures 2b and S5) and high-angle annular dark-field scanning transmission electron microscopy (HAADF-STEM) image (Figure 2c) reveal that rich, ultrasmall Pt HEA particles (indicated by yellow circles) with an average size of 3.36 nm (inset in Figure 2c) are uniformly distributed on the nearly transparent N−C matrix without aggregation. Then, the high-resolution TEM (HRTEM) image of a single Pt HEA particle in Figure 2d displays a distinct two-dimensional crystal lattice. The corresponding fast Fourier transform (FFT) pattern (Figure 2d inset) exhibits a characteristic diffraction pattern along the typical [011] crystallographic zone axis. This pattern shows two sets of crystalline planes of (200) and (11$\bar{1}$), marked with green and red stripes, respectively. Furthermore, Figure 2e,f present the inverse fast Fourier transform (IFFT) patterns derived from the (200) and (11$\bar{1}$) basal planes, respectively. The

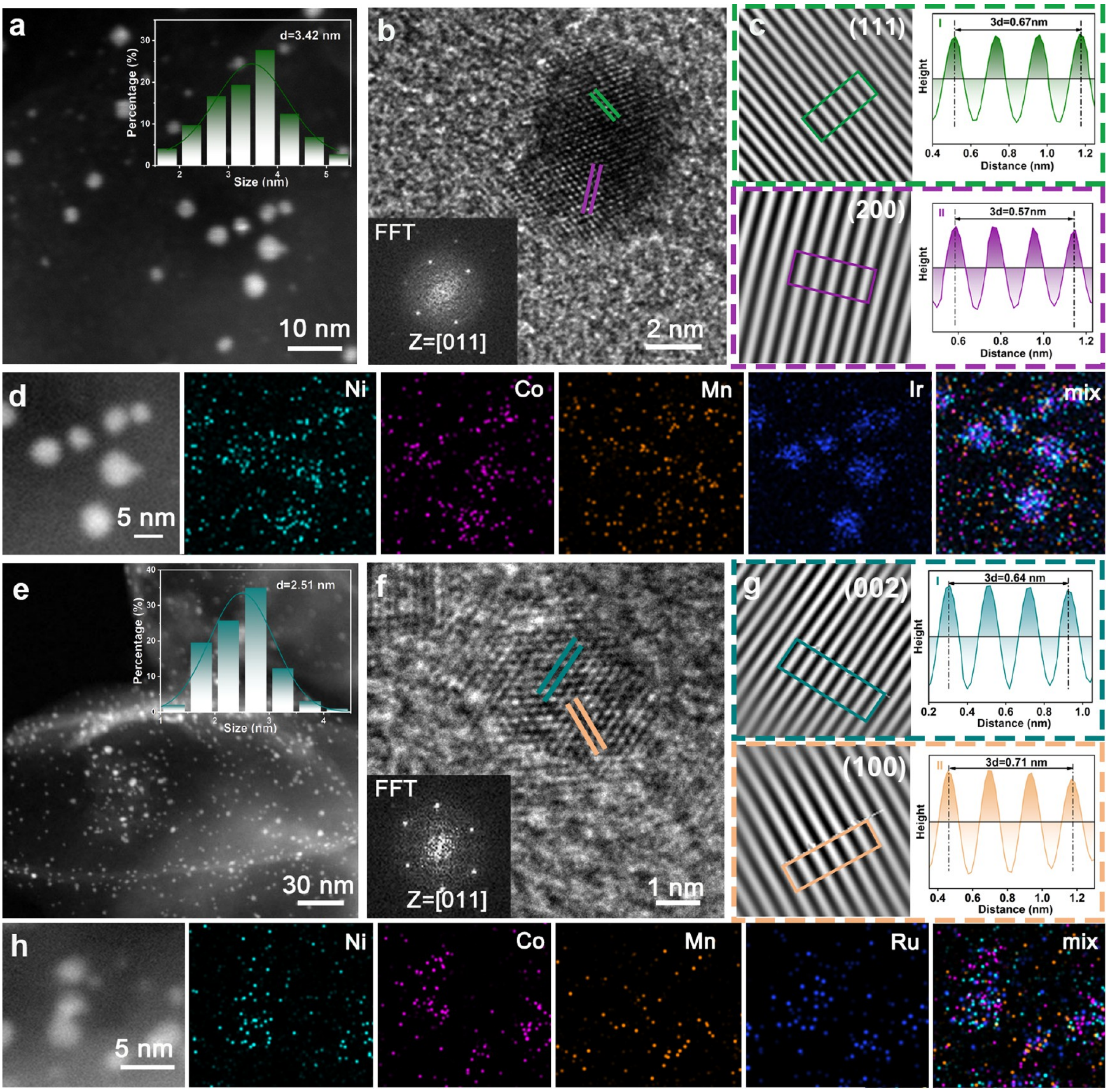

Figure 3. Morphology characterizations of Ir HEA@N−C and Ru HEA@N−C. (a) HAADF-STEM image (inset, particle size distribution) and (b) HRTEM image of Ir HEA@N−C (inset, FFT of the Ir HEA nanoparticle). (c) IFFT image and crystallite gaps diagram of the (111), (200) plane of the Ir HEA nanoparticle. (d) Elemental mapping images of Ir HEA@N−C. (e) HAADF-STEM image (inset, particle size distribution) and (f) HRTEM image of Ru HEA@N−C (inset, FFT of the Ru HEA nanoparticle). (g) IFFT image and crystallite gaps diagram of the (002), (100) plane of the Ru HEA nanoparticle. (h) Elemental mapping images of Ru HEA@N−C.

corresponding interplanar spacings of (200) and (11$\bar{1}$) are determined to be 0.197 and 0.227 nm, respectively. These spacings correspond to 3 and 10% contraction, respectively, when compared to that of Pt@N−C. This observed phenomenon primarily stems from the variation in the atomic radius of different metallic elements and the rapid heating−quenching rate during coreduction, which induces abundant lattice strain, thereby generating numerous dislocation defects in Pt HEA@N−C.[25−27] This can be further substantiated by geometrical phase analysis (GPA), as illustrated in Figure 2g,h.

High-magnification HAADF-STEM characterizations were then conducted to disclose the elaborate atom arrangement in the Pt HEA solid solution alloy. The representative HAADF-STEM images along the [001] zone axis of Pt HEA@N−C (Figure 2i,j) and the FFT pattern (inset) show that the Pt HEA nanocrystal features a typical face-centered cubic (fcc) structure. According to the large Z-contrast between the heavier Pt (195.1) and the lighter Ni (58.7), Co (58.9), and Mn (54.9), all of the atomic column arrangements do not show distinct periodic light and shade contrast, which indicates that the Pt atoms are randomly coordinated with the surrounding Ni, Co,

https://doi.org/10.1021/acsnano.5c00704

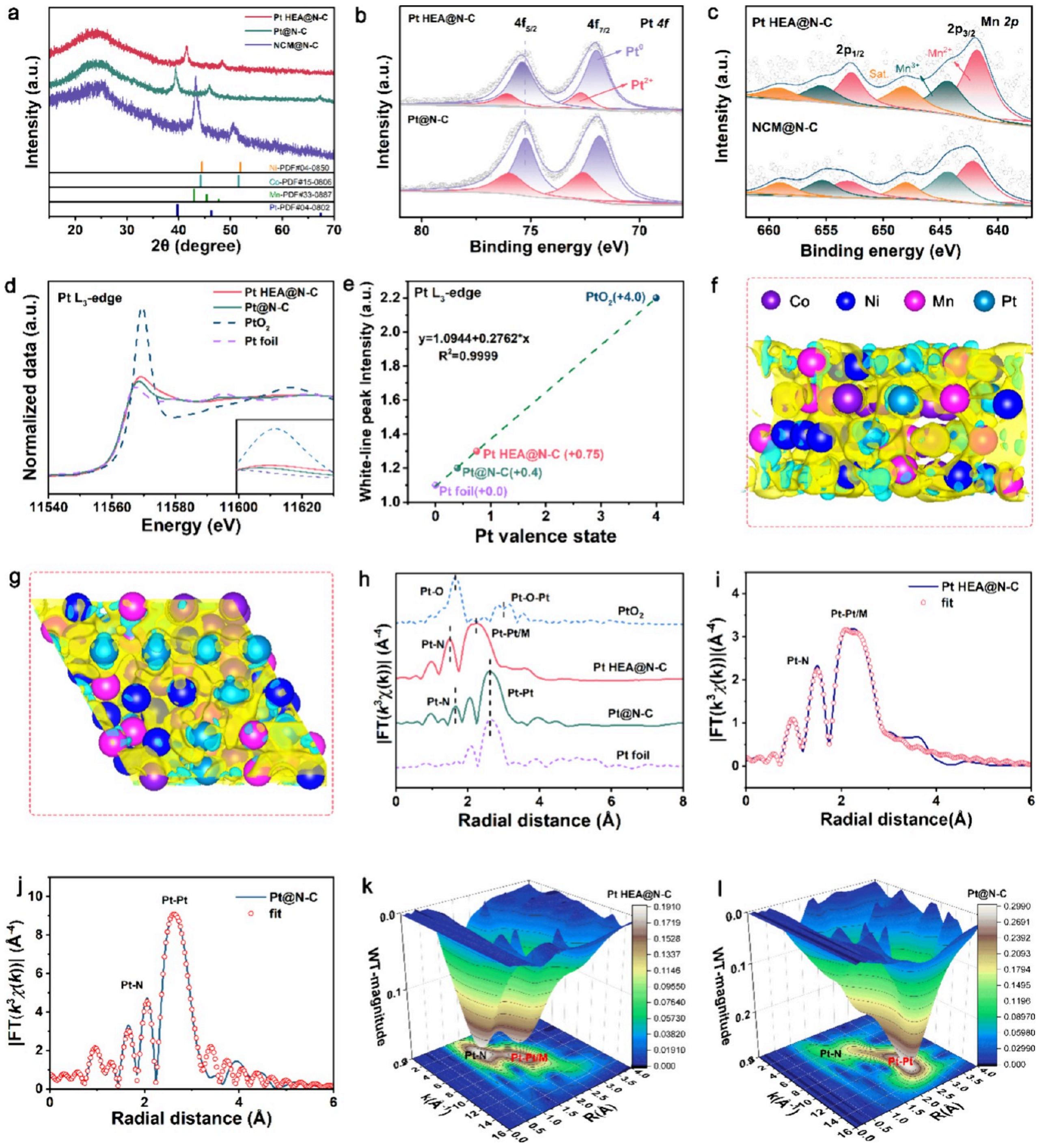

Figure 4. Structural characterizations of Pt HEA@N−C, Pt@N−C, and NCM@N−C. (a) XRD patterns of Pt HEA@N−C, Pt@N−C, and NCM@N−C. High-resolution XPS spectra of (b) Pt 4f and (c) Mn 2p. (d) Normalized L_3-edge XANES spectra of Pt HEA@N−C, Pt@N−C, PtO_2, and Pt foil. (e) Fitted Pt valences in Pt HEA@N−C and Pt@N−C. (f, g) Side view and front view of the charge density difference images within Pt HEA. Yellow and cyan contours represent electron accumulation and depletion, respectively, where the isosurface is set to be 0.005 e $bohr^{-3}$. (h) L_3-edge FT-EXAFS spectra in the R-space for Pt HEA@N−C, Pt@N−C, PtO_2, and Pt foil. Corresponding EXAFS fitting curves at the R-space for (i) Pt HEA@N−C and (j) Pt@N−C. WT-EXAFS analyses of (k) Pt HEA@N−C and (l) Pt@N−C.

and Mn atoms without composition and phase segregation. These results imply that due to the forceful multimetal diffusion and entropy stabilization effect from the rapid Joule heating under a high temperature of 900 °C, it is more feasible for the four metal elements to migrate and realize a self-assembled single-phase alloy structure with high configuration entropy. Furthermore, according to the 2D and 3D intensity distributions (Figures S6 and 2k), the Pt, Ni, Co, and Mn atoms can be observed to be disorderly distributed within a single solid solution phase. To elucidate the elemental distribution within Pt HEA@N−C, analyses of the line intensity distribution and elemental mapping were conducted. The line intensity distributions for two separate Pt HEA nanoparticles reveal heightened responses for the Pt, Ni, Co, and Mn elements (Figure 2l). Both elemental mappings composed of several HEA nanoparticles (Figure 2m) and an independent nanoparticle

(Figure S7) also ascertain the presence and uniform distribution of Pt, Ni, Co, and Mn atoms across the multiple alloy nanoparticle, further attesting to the successful synthesis of Pt HEA@N−C. Particularly, as illustrated in Figure S8, the Pt HEA@N−C catalyst possesses a large specific surface area of 261.36 m^2 g^{-1} and a mesopore-rich structure characterized by typical type IV isothermal attributes, conducive to the rapid charge transfer and efficient mass transport. Then, Raman spectra in Figure S9 reveal a modest rise in the D-to-G peak ratio after the incorporation of Pt, Ni, Co, and Mn metal components on the carbon substrate. Such changes hint at the formation of local defects within the Pt HEA@N−C matrix, contributing to enhancing its intrinsic electronic conductivity.

More importantly, our experimental strategy based on ternary lithium-ion battery recovery and the rapid Joule heating strategy can be expanded to other HEA-based catalysts. Therefore, the Ir HEA@N−C and Ru HEA@N−C composites were also fabricated in a general manner. The SEM and TEM images in Figure S10 reveal that the 2D ultrathin nanosheet morphology of N−C can still be well maintained, on the surface of which the ultrasmall Ir HEA nanoparticles are distributed widely throughout the carbon matrix, respectively, without any agglomeration. Moreover, for Ir HEA@N−C, the HAADF-STEM image in Figure 3a and the corresponding particle size distribution curve (inset) reveal an average particle size of 3.42 nm for Ir HEA. The TEM (Figure S10), HRTEM (Figure 3b), and IFFT results (Figure 3c) along the [011] zone axis of Ir HEA@N−C confirm the respective fcc lattice structures with lattice fringes of 0.23 and 0.19 nm aligning with the (111) and (200) crystal facets, respectively. Together with the XRD (Figure S11), EDS mapping (Figure 3d), and line scanning results (Figure S12a,b), it can be concluded that Ir, Ni, Co, and Mn atoms can also successfully migrate into the HEA *fcc* crystal lattice. Likewise, for Ru HEA@N−C, the HAADF-STEM (Figure 3e), HRTEM (Figures 3f and S13), IFFT (Figure 3g), mapping results (Figure 3h), and EDS line scanning profiles (Figure S12c,d) demonstrate the hexagonal-phase Ru HEA with a smaller mean particle size of 2.51 nm, and exposed crystal planes of (100) and (002) can be successfully obtained. At this point, it can be concluded that the unique second-level Joule heating approach plays a critical role in limiting further growth, coalescence, and agglomeration of the HEA nanoparticles with ultrasmall dimensions during synthesis. It is mentioned that according to the comparison of electrochemical properties, the Pt HEA@N−C catalyst is more effective in enhancing the round-trip efficiency relative to that of Ir HEA@N−C and Ru HEA@N−C, which will be discussed later. In this regard, the Pt HEA@N−C catalyst is selected to further illustrate the critical role of reverse electron transfer and intense multielement synergy in boosting the bifunctional reaction kinetics of $Li-O_2$ batteries.

Electronic Structure Characterization. The crystal structures of Pt HEA@N−C, Pt@N−C, and NCM@N−C were then analyzed by X-ray diffraction (XRD). As shown in Figure 4a, the diffraction peaks of Pt@N−C at 39.8°, 46.2°, and 67.5° correspond to the (111), (200), and (220) crystal planes of Pt (PDF#04-0802).[28,29] The two distinct diffraction peaks at 41.7° and 48.6° for Pt HEA@N−C are attributed to the (111) and (200) planes within the single-phase fcc structure in accordance with pure Pt. This further indicates the formation of a single-phase solid solution alloy without phase separation. It is mentioned that the diffraction peaks are down-shifted compared to NCM@N−C and up-shifted compared to Pt@N−C, indicating that the mutual replacement of Pt with Ni, Co, and Mn atoms with different atomic radii causes the distinct variation in crystallographic lattice constants. This further confirms the successful alloying within the disordered HEA structure. Furthermore, the diffraction peaks of Pt HEA@N−C possess a large full width at half-maximum and a low peak intensity, implying the Pt HEA nanoparticles feature a small dimension and a relatively low degree of crystallization. To explore the valence states and detailed coordination environment of metal elements, X-ray photoelectron spectroscopy (XPS) and X-ray absorption spectrum (XAS) were conducted. As shown in the high-resolution Pt 4f spectrum in Figure 4b, for Pt HEA@N−C, the peaks located at 72.02 and 75.40 eV correspond to Pt $4f_{7/2}$ and Pt $4f_{5/2}$, respectively, which exhibit a distinct movement toward higher binding energies relative to that of Pt $4f_{7/2}$ (71.96 eV) and Pt $4f_{5/2}$ (75.25 eV) for Pt@N−C.[30−32] The increased Pt valence state in Pt HEA@N−C is potentially due to the electronegativity differences in various metal sites. Notably, there exists a substantial electronic interaction between the Ni, Co, and Mn 3d orbitals and the Pt 5d orbital, leading to a pronounced electron-deficit effect at the Pt sites.[23] The corresponding situation is that compared with NCM@N−C, all of the Ni 2p (Figure S14a), Co 2p (Figure S14b), and Mn 2p (Figure 4c) peaks show a negative shift of about 0.30 eV in Pt HEA@N−C, suggesting that Ni, Co, and Mn atoms within the alloy incline to attract electrons from adjacent Pt and exist in an electron-rich state. More importantly, to verify the origin of the unconventional charge transfer, we have prepared a contrast sample, which was obtained by calcination in a tubular furnace for 3 h at the same temperature (Pt HEA@N−C-furnace). As shown in Figures S14 and S15, the Pt 4f binding energy of the Pt HEA@N−C-furnace is down-shifted relative to that of Pt@N−C, and the Ni 2p, Co2p, and Mn 2p binding energies are positively shifted, implying the traditional electron flow from Ni, Co, and Mn atoms to Pt, which demonstrate the opposite direction of electron transfer for the case of Pt HEA@N−C. Likewise, as shown in Figure S16a,b, the Ir HEA@N−C-furnace and Ru HEA@N−C-furnace demonstrate a similar binding energy change tendency. Based on these considerations, it is inferred that the traditional tube furnace heating method is not sufficient to drive charge transfer from Pt to Ni, Co, and Mn during reduction of metal salts and the alloying process due to its mild rise and fall in temperature. In sharp contrast, the second-scale heating−quenching conditions by the extreme Joule heating thermal shock play a critical role in driving reverse charge transfer. In detail, the Joule heating shockwaves with a much larger current value afford an extremely higher thermodynamic activation energy, triggering the controllable electron donation−acceptation direction to surmount the electronegativity obstacle during the in situ metal−metal coordination process within a single-phase solid solution alloy. This finally contributes to establishing a strong kinetically stabilized 3d−5d orbital interaction between the metal atoms and tuning the electron density states of the Pt sites. Such interesting interatomic interactions in Pt HEA@N−C facilitate the modulation of Pt electronic configurations, which are particularly suitable for enhancing intrinsic catalytic activity when used for $Li-O_2$ batteries.

The normalized X-ray absorption near-edge structure (XANES) spectrum for the L_3-edge of Pt (Figure 4d) reveals that both the white line peaks for Pt HEA@N−C and Pt@N−C are positioned between the reference Pt foil and PtO_2, but closer to the former one. This indicates the catalysts are dominated by

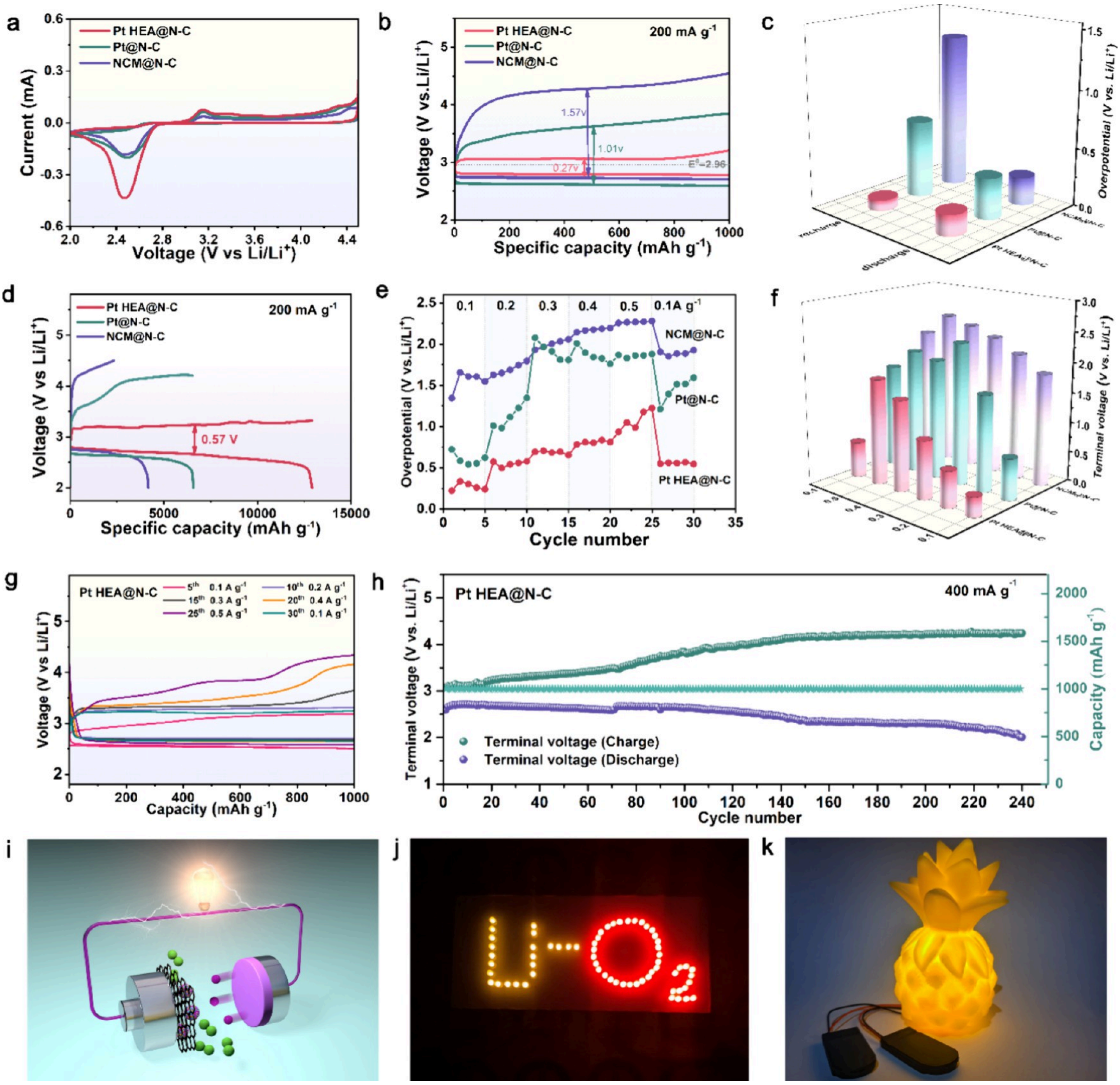

Figure 5. Electrochemical performance of Pt HEA@N−C, Pt@N−C, and NCM@N−C. (a) CV curves of Pt HEA@N−C, Pt@N−C, and NCM@N−C electrodes with a scanning rate of 0.1 mV s^{-1}. (b) Discharge−charge curves of the three electrodes with a cutoff capacity of 1000 mAh g^{-1} under 200 mA g^{-1}. (c) Summarized discharge and charge overpotentials in (b). (d) Initial deep discharge−charge profiles of the three electrodes at 200 mA g^{-1}. (e) Overpotentials of the three electrodes under different current densities from 0.1 to 0.5 A g^{-1} with a limited capacity of 1000 mAh g^{-1}. (f) End discharge and charge voltage gaps under different current densities for the three electrodes. (g) Discharge−charge curves under varying current densities of the Pt HEA@N−C electrode. (h) Cycling stability of the Pt HEA@N−C electrode at 400 mA g^{-1} under 1000 mAh g^{-1}. (i) Schematic configuration of the Li−O$_2$ battery. (j) Photograph of LEDs powered by the Pt HEA@N−C catalyst equipped with Li−air batteries. (k) A pineapple toy is successfully illuminated by the Pt HEA@N−C-based Li−air batteries.

metallic-state Pt, with the presence of positively charged Pt.[33−36] Importantly, the white line intensity of Pt HEA@N−C surpasses that of Pt@N−C, which offers direct proof of the apparently elevated oxidation state of Pt$^{\delta+}$ for the former one. Furthermore, as demonstrated in Figure 4e, the quantitative valence state of the Pt in Pt HEA@N−C is determined to be about +0.75 according to the fitting analysis by the white line intensity, which is larger than that of Pt@N−C (+0.4) and consistent with the XPS results. Moreover, in addition to experimental evidence, the theoretical charge density difference results by the first-principles calculations in Figure 4f (side view) and g (front view) disclose that the Pt sites with cyan contours feature apparent electron depletion and the Ni, Co, and Mn sites with yellow contours as an electron reservoir show electron accumulation, respectively. Hence, the calculation results support the possibility of unconventional electron transfer from Pt with a higher electronegativity to Ni, Co, and Mn with a smaller electronegativity during the electron rearrangement process, resulting in a fine-regulated d-electronic configuration for the active Pt sites. This is in good agreement with the XPS and XANES results. Moreover, as intuitively shown in the Fourier transform k^3-weighted extended X-ray absorption fine structure (FT-EXAFS) spectra for the Pt L_3-edge in R-space (Figure 4h) and k-space (Figure S17), both Pt HEA@N−C and Pt@N−C display two noticeable coordination peaks with multiple coordination metal elements in the first shell. For Pt HEA@N−C, the weaker peak situated at about 1.50 Å (nonphase-corrected) is ascribed to the Pt−N scattering path, indicating the efficient HEA−support interaction. The stronger peak at about 2.24 Å (nonphase-corrected) is attributed to the Pt−Ni/Co/Mn/Pt scattering path in HEA@N−C. In sharp contrast, for Pt@N−C, the stronger peak at about 2.61 Å (nonphase-corrected) assigned to the Pt−Pt scattering path is much closer to that of the bulk Pt foil reference and much larger than that of Pt HEA@N−C. This indicates that relative to Pt@N−C and the Pt foil, the coordination environment of Pt in Pt HEA@N−C is fundamentally changed after incorporation of alien Ni, Co, and Mn atoms within the Pt fcc lattice. According to the quantitative fitting results of FT-EXAFS spectra for Pt L_3-edge by least-squares in R-space (Figure 4i,j), k-space (Figures S18 and S19), and Table S2, for Pt HEA@N−C, the Pt−metal coordination in the first shell can be ascribed to the contribution from Pt−Ni/Co/Mn with the average bond length of 2.54 Å and from Pt−Ni/Co/Mn/Pt with the average bond length of 2.66 Å, respectively, which suggest a disordered, high-entropy coordination structure. By contrast, the Pt−Pt bond length in Pt@N−C is fitted as 2.75 Å, which is much larger than PtM in Pt HEA@N−C. Hence, the shortened interatomic distances further indicate the successful coordination between Pt and Ni, Co, and Mn in the latter random alloy. Additionally, the coordination number (CN) for the Pt−Ni/Co/Mn and Pt−Ni/Co/Mn/Pt bonds in Pt HEA@N−C was determined to be 2.8 and 3.0, respectively, in contrast to a Pt−Pt CN value of 6.1 for Pt@N−C. This change can be attributed to the completely different high-entropy distribution in Pt HEA relative to the well-ordered single-element Pt nanoparticle. Concurrently, as summarized in the wavelet transform (WT) analysis on R-space and k-space (Figures 4k,l and S20), the XANES and FT-EXAFS results support the homogeneous multielement miscibility of Pt, Ni, Co, and Mn with different physiochemical characteristics within the single fcc HEA nanoparticle. This well-designed high-entropy configuration effect in Pt HEA@N−C is energy favorable for tuning the d orbital electrons and coordination environment of Pt and thus deeply optimizing the adsorption state of oxygen-related intermediate products. Therefore, the rich activated catalytic sites are expected to enhance the ORR/OER electrocatalytic performance of Li−O_2 batteries.

Electrocatalytic Performance. A series of electrochemistry experiments were then undertaken to assess the distinctive catalytic function of Pt HEA@N−C with the high-entropy compositional design in boosting the catalytic efficacy of Li−O_2 batteries. Figure 5a illustrates the cyclic voltammetry (CV) curves of the three catalysts at a scan rate of 0.1 mV s^{-1} over potentials ranging from 2.0 to 4.5 V (versus Li/Li^+). It is clear that in spite of the similar reduction peak position during ORR ($O_2 + 2Li^+ + 2e^- \rightarrow Li_2O_2$), the Pt HEA@N−C electrode demonstrates much enhanced reduction peak currents and integral area compared to Pt@N−C and NCM@N−C. This signifies the higher amount of generated Li_2O_2 and a larger discharge capacity for the former electrode.[1,37−39] Furthermore, the Pt HEA@N−C electrode possesses an elevated ORR onset potential during the cathodic scan and a reduced OER onset potential during the anodic scan. This implies that by adjusting the intermediate adsorption energy at the Pt sites via the recovered Ni, Co, and Mn boosting effects within Pt HEA@N−C, there is a facilitated formation ($O_2 + 2Li^+ + 2e^- \rightarrow Li_2O_2$) and efficient decomposition ($Li_2O_2 \rightarrow O_2 + 2Li^+ + 2e^-$) of Li_2O_2, demonstrating its faster dynamic response and ameliorated O_2 redox efficiency. Furthermore, Figure 5b displays the galvanostatic discharge and charge profiles of the three electrodes at a fixed capacity of 1000 mAh g^{-1} and a current density of 200 mA g^{-1}. Notably, the Li−O_2 batteries assembled with the Pt HEA@N−C electrode present an exceptionally low overall overpotential of 0.27 V, during which the discharge and charge polarizations are reduced to just 0.18 and 0.09 V, respectively, with an energy efficiency of up to 91.1%. This is among the best-reported catalysts for Li−O_2 batteries. In contrast, the Pt@N−C and NCM@N−C electrodes exhibit much larger overpotentials of 1.01 V (ORR: 0.35 V; OER: 0.66 V; energy efficiency: 72.1%) and 1.57 V (ORR: 0.24 V; OER: 1.33 V; energy efficiency: 63.4%), respectively. The much-enhanced dual-functional catalytic performance indicates that the incorporation of surrounding Ni, Co, and Mn atoms not only fully activates the ORR kinetics of Pt sites but also facilitates the OER catalytic activity within Pt HEA@N−C. This disparity also suggests the different formation-decomposition mechanisms of Li_2O_2 in the Pt HEA@N−C cathode compared to its counterparts, enabling the efficient reversible transformation of Li_2O_2 during the O_2 redox process due to its enhanced catalytic capability. A bar graph in Figure 5c offers a more lucid comparison of the discharge, charge, and overall overpotentials among the three electrodes, further emphasizing the distinct advantages of the Pt HEA@N−C cathode in improving the O_2 redox reactions. Meanwhile, as shown in Figure S21, the well-designed Ir HEA@N−C and Ru HEA@N−C hybrids also harvest low polarization of 0.63 and 1.36 V, respectively. However, they are still larger than that of Pt HEA@N−C. Considering the similar morphology characteristic and structure composition of the three catalysts, the enhanced energy efficiency of the latter may derive from the optimized electronic structure of Pt active sites and the appropriate adsorption strength toward oxygen-involved intermediates. This makes Pt HEA@N−C with a superior intrinsic catalytic activity more feasible for accelerating the reversible transformation of the Li_2O_2 species during ORR and OER, thus achieving ameliorated overall polarization relative to that of the Ir HEA@N−C and Ru HEA@N−C counterparts. Specifically, the galvanostatic discharge/charge curves of the catalysts obtained by calcination in a tubular furnace were also tested. As shown in Figure S22, all of the overpotentials of the Pt HEA@N−C-furnace (1.61 V), Ir HEA@N−C-furnace (1.62 V), and Ru HEA@N−C-furnace (1.64 V) are distinctly increased when compared with the Pt HEA@N−C, Ir HEA@N−C, and Ru HEA@N−C counterparts. These results further indicate the advantages of the unique reverse electron transfer mechanism and high-entropy coordination configuration in fully motivating the intrinsic catalytic capability of Pt in Pt HEA@N−C to be more suitable for driving Li−O_2 batteries, which break through the electronegativity limitation and facilitate bifunctional catalytic kinetics.

Then, the constant-current charge/discharge curves at a current density of 200 mA g^{-1} within the voltage of 2.0−4.5 V in Figure 5d depict that the Pt HEA@N−C electrode harvests a deep discharge/recharge capacity of 12917.4 mAh g^{-1} with an impressive Coulombic efficiency of 100%. Although the Pt@N−

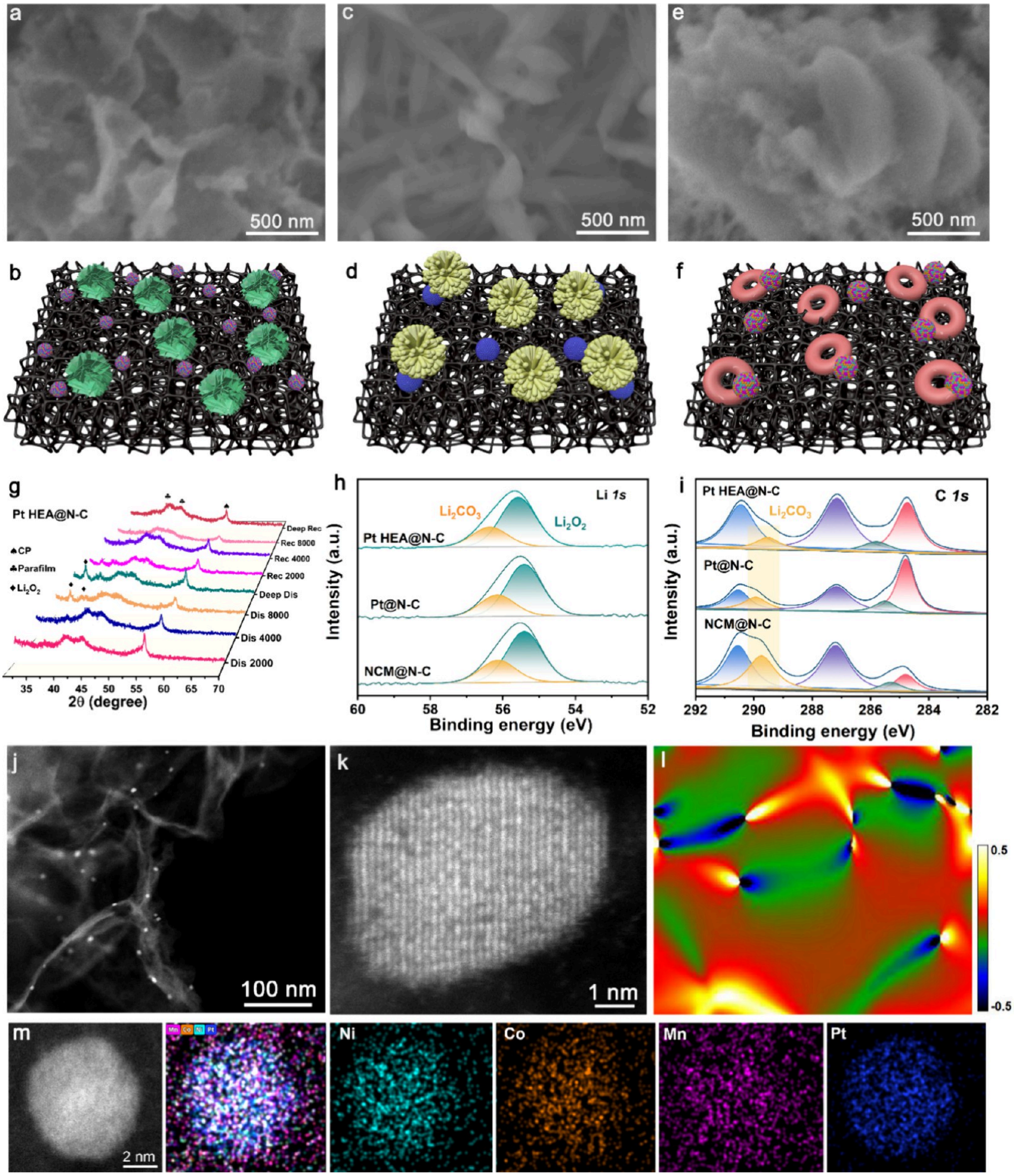

Figure 6. Ex situ characterizations of the discharged and charged electrodes. Ex situ SEM images and simulated schematic illustration of the full discharged (a, b) Pt HEA@N−C, (c, d) Pt@N−C, and (e, f) NCM@N−C. (g) Ex situ XRD patterns of charged and discharged Pt HEA@N−C at different stages during the first cycle. Ex situ XPS spectra of the discharged Pt HEA@N−C, Pt@N−C, and NCM@N−C electrode in (h) Li 1s and (i) C 1s regions at the 30th cycle. (j, k) Ex situ HAADF-STEM images, (l) GPA results, and (m) elemental mapping of the 200th cycled Pt HEA@N−C catalyst.

C electrode achieves the same Coulombic efficiency, the discharge/recharge capacities are only 6584.2 mAh g^{-1}. Moreover, NCM@N−C achieves much lower capacities of 4174.3 and 2336.9 mAh g^{-1}, respectively, with a Coulombic efficiency of only 55.9%. In addition, the Pt HEA@N−C cathode demonstrates a stable voltage plateau during the ORR and OER processes. Especially, for OER, Pt HEA@N−C outputs its nearly whole charge capacity at a very low voltage plateau of about 3.12 V until the Coulombic efficiency reaches 100%. By contrast, Pt@N−C shows two different charging zones of 2.96−4.12 V with a capacity contribution rate of 50.9% and 4.12−4.21 V with a capacity contribution rate of 49.1%. More critically, for NCM@N−C, the charge voltages increase instantly to 4.19 V upon OER and then climb to 4.5 V without an apparent charge plateau. These results correspond to the absolute decomposition characteristics of the as-generated Li_2O_2 species. As summarized in Figure S23, the overall voltage gap of Pt HEA@N−C is as low as 0.57 V, which is significantly lower than that of Pt@N−C (1.51 V) and NCM@N−C (1.60 V). This further indicates that, relative to the counterparts, the well-tuned Pt HEA@N−C electrode with the pronounced reverse electron transfer and high-entropy coordination effects definitely possesses more efficient formation and decomposition efficiency toward Li_2O_2.

Next, the rate capabilities of the three electrodes at various current densities of 100, 200, 300, 400, and 500 mA g^{-1} with a cutoff capacity of 1000 mAh g^{-1} were evaluated. As demonstrated in Figures 5e−g and S24, Pt HEA@N−C achieves slight voltage fluctuations and much smaller voltage hysteresis compared with Pt@N−C and NCM@N−C under both small and large current densities. For Pt HEA@N−C, the terminated ORR and OER potentials are 2.58 and 4.34 V under 500 mA g^{-1}, respectively, with a smaller polarization of 1.76 V. In sharp contrast, although Pt@N−C can maintain low overpotentials at a smaller current density, its polarization values rise quickly as the current density increases, manifesting the serious activity decay. For example, the ORR and OER ending potentials of Pt@N−C are 2.47 and 4.53 V under 500 mA g^{-1}, respectively, outputting a much larger polarization of 2.06 V. For the NCM@N−C reference, the charging cutoff voltage even exceeds 4.5 V, indicating inferior high-rate performance. However, for Pt HEA@N−C, the charging cutoff voltage can still be below 4.35 V with outstanding high-rate catalytic kinetics and reliability. It is mentioned that when the current density is reverted to 100 mA g^{-1}, the charge/discharge overpotential of Pt HEA@N−C decreases to a low value of 0.55 V, which is superior to that of Pt@N−C (1.60 V) and NCM@N−C (1.93 V), further underscoring the superior catalytic stability and substantially enhanced reversibility of the Pt HEA@N−C electrode under diverse current densities. Then, the cycling stability of the three cathodes under 200 mA g^{-1} with a cutoff capacity of 500 mAh g^{-1} and 400 mA g^{-1} with a cutoff capacity of 1000 mAh g^{-1} was evaluated. As shown in the galvanostatic discharge/charge profiles (Figure S25), the Pt HEA@N−C-equipped Li−O_2 batteries can steadily run for 355 cycles under 200 mA g^{-1} with a cutoff capacity of 500 mAh g^{-1}, significantly higher than that of Pt@N−C (200 cycles) and NCM@N−C (96 cycles). As shown in Figure 5h, when cycling at 400 mA g^{-1} with a cutoff capacity of 1000 mAh g^{-1}, the Pt HEA@N−C cathode still harvests a superior lifespan up to 240 cycles. More importantly, its charging voltage can be controlled at a lower value throughout the cycling process, which is crucial for inhibiting the production of a significant number of harmful byproducts. By contrast, the Pt@N−C and NCM@N−C counterparts can operate for only 164 and 83 cycles, respectively (Figure S26). The much-reduced discharge/charge polarization, superb rate performance, and prolonged cycling life of Pt HEA@N−C further highlight the critical role of the reverse electron transfer and high-entropy coordination effects in optimizing the nucleation and decomposition behaviors of the Li_2O_2 species, which directly contribute to enhancing the catalytic kinetics and energy efficiency. Meanwhile, as shown in Table S3, the charge−discharge polarization and cycling life comparisons of the Pt HEA@N−C catalyst with those recently reported noble-metal-involved hybrids clearly indicate its remarkable superiority in expediting electrocatalytic kinetics for Li−O_2 batteries. Furthermore, the Pt HEA@N−C catalyst based on the fresh cathode material was also fabricated. As shown in Figure S27, the Pt HEA@N−C-fresh catalyst also harvests an ultralow charge and discharge overpotential of 0.29 V, which is close to that of Pt HEA@N−C. Its excellent catalytic activity further demonstrates the competitive economic value and application prospect of our innovative strategy of upcycling valuable metals based on waste lithium-ion batteries into efficient HEA catalysts. Furthermore, the electrochemical impedance spectra (EIS) for the Pt HEA@N−C, Pt@N−C, and NCM@N−C cathodes in Figure S28 reflect a smaller semicircle at a high frequency for Pt HEA@N−C associated with charge transfer resistance, implying its advantage in accelerating electron transfer capability between Li_2O_2 and the catalytic cathode.[40] Then, as shown in Figure 5i,j and S29, eight Li−air coin batteries equipped with the Pt HEA@N−C cathodes connected in parallel successfully illuminate a homemade light-emitting diode (LED) with letter arrays of Li−O_2. It can maintain brightness for 3 h without luminance attenuation (Figure S30). Additionally, a pineapple toy is successfully illuminated using just four Pt HEA@N−C Li−air cells (Figure 5k). The aforementioned results not only demonstrate the feasibility of the Pt HEA@N−C-equipped Li−O_2 battery system for practical application but also highlight its great potential in terms of energy utilization efficiency and superior durability. Furthermore, this research realizes a new concept of recycling waste lithium-ion batteries and breaks through the design bottleneck of traditional catalysts. Our strategy, based on the fresh reverse charge transfer and high-entropy stabilization mechanism, not only provides a new idea for the catalyst construction for lithium−oxygen batteries but also advances its application scope for versatile electrocatalysis fields, such as Li−CO_2 batteries, Zn−air batteries, water splitting, and so on, which also demand high-efficiency dual-functional catalysts.

Microstructure Evolution of Electrodes after ORR/OER. To elucidate the reasons why the Pt HEA@N−C catalyst can significantly improve the electrochemical performance of Li−O_2 batteries, we have deeply explored the corresponding ORR/OER mechanisms by systematically analyzing the microstructural changes of Li_2O_2 during its generation and decomposition processes, which help understand the complexity of this battery system. The microstructures of the postcharged and discharged Pt HEA@N−C, Pt@N−C, and NCM@N−C cathodes were first meticulously studied using ex situ SEM. As shown in the SEM image (Figure 6a) and its schematic model (Figure 6b), after deep discharge, the Pt HEA@N−C cathode surface is evenly coated with abundant petal-like Li_2O_2 accommodates assembled with stacked ultrathin nanosheets. This unique Li_2O_2 species not only mitigates active site obstruction on the electrode surface but also contributes to providing an increased three-phase interface, which is associated with the notable enhancement in the discharge capacity of Pt HEA@N−C. More importantly, as certified by Figure S31, the surface of the Pt HEA@N−C catalyst can be well-recovered without discharge product residues. This indicates that the well-contacted Li_2O_2/electrolyte/electrode interface, the ameliorated utilization efficiency of catalytic sites, and the rapid oxygen release pathway benefit the continuous high-efficiency conversion of Li_2O_2 into O_2. This process facilitates the swift and complete decomposition of Li_2O_2, restoring the active catalytic surface to its original state for Pt HEA@N−C. Finally, this mechanism results in a much-reduced polarization voltage and enhanced Coulombic efficiency for the Pt HEA@N−C electrode. In sharp contrast, as shown in Figure 6c−f, the

https://doi.org/10.1021/acsnano.5c00704

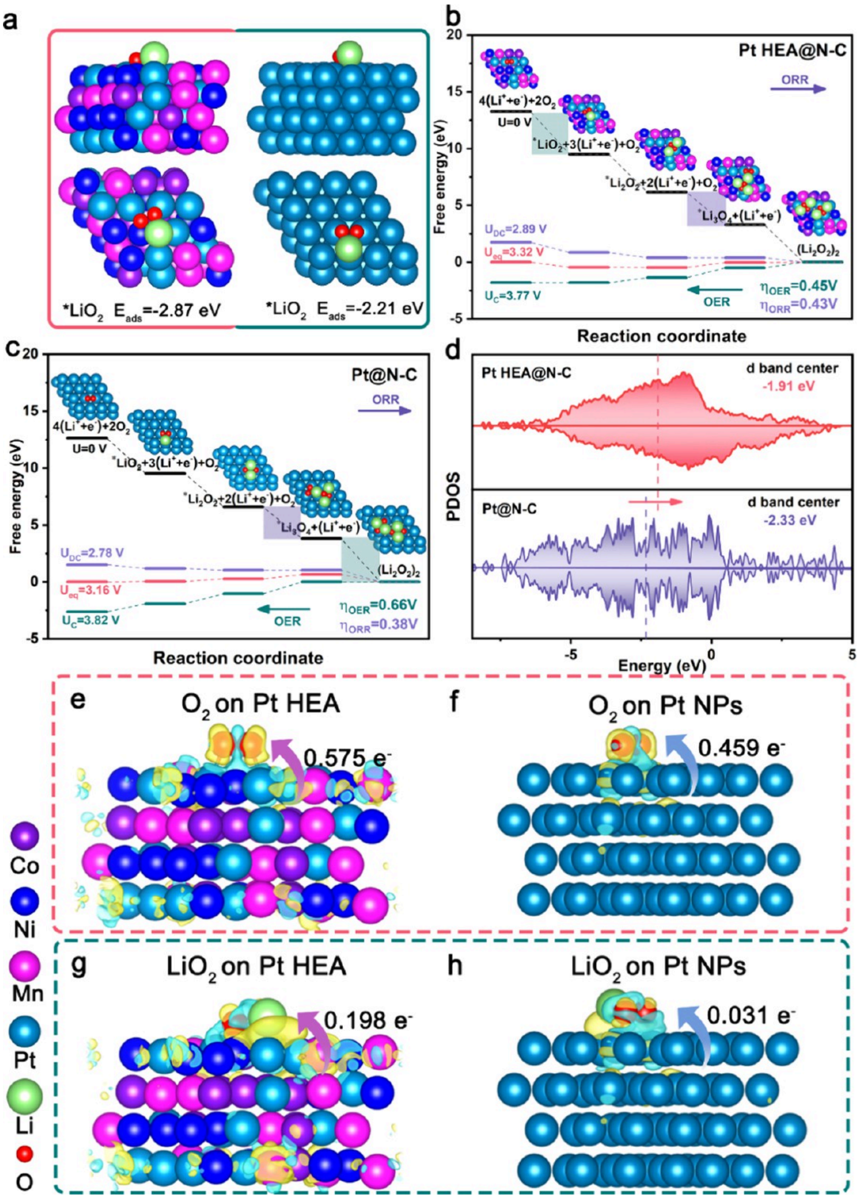

Figure 7. DFT calculations. (a) Comparison of the LiO_2 adsorption energies of Pt HEA and Pt NPs. Gibbs free energy diagram of (b) Pt HEA and (c) Pt NPs. (d) PDOS of Pt HEA and Pt NPs. Side view of the charge density difference plots of O_2 on (e) Pt HEA and (f) Pt NPs. Side view of the charge density difference plots of LiO_2 on (g) Pt HEA and (h) Pt NPs. Yellow and cyan contours represent electron accumulation and depletion, respectively, where the isosurface is set to be 0.002 e bohr^{-3}.

electrode surfaces of Pt@N−C and NCM@N−C are covered with numerous rods and discs of Li_2O_2, respectively, which weaken the interfacial contact between the catalysts and discharge products, leading to increased mass-transfer resistance. This obstruction in Li^+ and O_2 transport hinders timely Li_2O_2 decomposition, causing incomplete oxygen release reactions or even deactivation on the electrode surface, thereby deteriorating the round-trip efficiency.[41−43] As verified in the SEM images of the recharged Pt@N−C and NCM@N−C (Figure S32a,b), the accumulation of a large amount of Li_2O_2 necessitates higher energy for complete decomposition, contributing to an increase in the level of OER polarization. Herein, our findings indicate that the reclaimed Ni, Co, and Mn atoms as electron acceptors and the high-entropy activation component fundamentally tune the adsorption strength of the neighboring Pt centers of Pt HEA@N−C toward oxygen-involved intermediates, thus manipulating the morphology, distribution of the oxygenated Li_2O_2 products, as well as the three-phase interface. Then, the optimized Li_2O_2 with decomposition reversibility consequently contributes to enhancing the overall ORR/OER performance of Pt HEA@N−C.

Furthermore, as shown in Figure 6g, the ex situ XRD patterns of the Pt HEA@N−C cathode at different discharge processes (2000, 4000, 8000 mAh g^{-1}, deep discharge) and the following charging processes (2000, 4000, 8000 mAh g^{-1}, deep recharge) were also recorded. This component analysis reveals the presence of characteristic Li_2O_2 diffraction peaks (PDF#09-0355) without any detectable signals from byproducts, suggesting Li_2O_2 is the predominant discharge product for Pt HEA@N−C during ORR.[7,44−46] Notably, the Li_2O_2 peaks associated with the Pt HEA@N−C electrode surface are less intense and can be rapidly diminished during recharge. This behavior is likely due to the reduced crystallinity of the ultrathin petal-like Li_2O_2, which facilitates its formation and decomposition efficiency during ORR/OER, underscoring its superior transformation reversibility on the Pt HEA@N−C cathode. On the other hand, distinct Li_2O_2 diffraction peaks with strong intensity can be observed for the Pt@N−C and NCM@N−C cathodes after full discharge (Figure S33a,b). It is mentioned that these peaks remain visible even after full recharge, indicating the incomplete decomposition of Li_2O_2, consistent with the ex situ SEM results in Figure S32a,b. The gradual accumulation of the electrically insulating Li_2O_2 would induce surface passivation, increased redox polarization, and thus undesirable parasitic reaction, which can be further confirmed by the ex situ XPS characterizations of the cycled electrodes. As shown in Li 1s spectra of the three cathodes at the 30th discharged state in Figure 6h, the fitted peak signals at about 55.4 and 56.1 eV are attributed to Li_2O_2 and Li_2CO_3, respectively. According to the fitted peak integration area, the Li_2CO_3 contents on the surface of the Pt HEA@N−C, Pt@N−C, and NCM@N−C electrodes are quantitatively determined to be about 28.2, 29.8, and 31.6%, respectively. The dominant amount of Li_2O_2 species for the discharged Pt HEA@N−C cathode indicates its superior resistance to production and accumulation of the side-products due to the ultrasmall overpotential and boosted energy conversion efficiency during cycling. More obviously, further examinations of the C 1s spectra in Figure 6i reveal that the 30th discharged Pt HEA@N−C cathode demonstrates negligible amounts of Li_2CO_3. However, this is not the case for the Pt@N−C and NCM@N−C cathodes, which output significant signals of Li_2CO_3, further highlighting the enhanced performance of the Pt HEA@N−C cathode in minimizing byproduct accumulation. It is noteworthy that the persistent accumulation of byproducts obstructs the electron and mass transport pathways, thereby increasing the electrical resistance and ultimately leading to a fast decline of the redox efficiency and operational life of Pt@N−C and NCM@N−C in Li−O_2 batteries.[47] To assess the long-term stability, we also characterized the detailed microstructure of the Pt HEA@N−C catalyst after 200 cycles. The ex situ HAADF-STEM image in Figure 6j illustrates that even after repeated redox cycling in a strong oxidative electrolyte, the Pt HEA nanoparticles are still homogeneously scattered on the whole carbon matrix, demonstrating the excellent antidecomposition and antiagglomeration capabilities of the Pt HEA@N−C catalyst. Furthermore, the high-resolution HAADF-STEM image of Pt HEA@N−C in Figures 6k and S34 still shows distinct (111) and (200) planes of the Pt HEA nanoparticle with lattice spacings of 2.85 and 1.92 Å, respectively. Meanwhile, according to the GPA strain map of an individual Pt HEA nanoparticle (Figure 6l), apparent lattice deformation and robust stretching-compressing strain can still be well observed within the nanoalloy, which plays a crucial role in maintaining stable electrocatalytic activity under long-term working conditions. Furthermore, the EDS elemental mapping in Figure 6m shows that the Pt, Ni, Co, and Mn elements in the 200th cycled Pt HEA@N−C catalyst remain uniformly distributed after long-term cycling without agglomeration or dissociation. These ex situ characterizations jointly highlight the outstanding long-period structural and compositional stability of Pt HEA@N−C, which can be attributed to the robust high-entropy stabilization effect in the single-phase *fcc* solid solution alloy structure.

DFT Calculations for Mechanism Analysis. To further clarify that the ORR/OER redox mechanisms in Li−O_2 batteries involve multiple chemical pathways for the reversible conversion of intermediates, in-depth DFT calculations were performed. To disclose the crucial role of Ni, Co, and Mn atoms in activating the intrinsic catalytic kinetics of Pt, both the optimized structures of Pt HEA and pure Pt nanoparticles (NPs) with the (111) surface are established as shown in Figure S35. It is mentioned that during the ORR process, O_2 molecules are first adsorbed on the cathode to undergo a one-electron reduction process, reacting with Li^+ at the three-phase interface to form a LiO_2 intermediate ($Li^+ + e^- + O_2 \rightarrow LiO_2$). Therefore, the adsorption characteristics of the O_2 reactant and the LiO_2 intermediate on the catalyst surface as important factors determine the subsequent nucleation and growth process of the Li_2O_2 discharge products. Herein, as shown in the O_2 adsorption structures (side view and top view) on the substrates (Figures S36 and S37), the Pt HEA catalyst demonstrates a higher binding energy (ΔE_{ads}) of −1.73 eV compared with pure Pt (−0.91 eV). This indicates that the Pt HEA catalyst with a stronger O_2 affinity facilitates the O−O bond breakage and accelerates the rate of reduction of O_2 upon ORR. Similarly, for the case of LiO_2 adsorption, as shown in Figure 7a, Pt HEA is conducive to binding firmly with the intermediates with a higher adsorption energy of −2.87 eV than that of pure Pt (−2.21 eV), which significantly alters the growth mode of Li_2O_2. Considering the different discharge product morphologies of Pt HEA@N−C and Pt@N−C, it is speculated that due to stronger affinity, it preferentially realizes a secondary electron transfer process on the Pt HEA surface for the following Li_2O_2 growth ($LiO_2 + e^- + Li^+ \rightarrow Li_2O_2$), inducing the formation of nanoflower-like Li_2O_2 deposited on the cathode surface with preferable interface compatibility, which has been experimentally verified with better decomposition efficiency and feasibility during the OER. With regard to the pure Pt NPs with a lower adsorption energy, the LiO_2 intermediates have a tendency to release into the electrolyte and then undergo a disproportionation reaction ($2LiO_2 \rightarrow Li_2O_2 + O_2$), resulting in the formation of rod-shaped Li_2O_2, which takes more energy to be fully decomposed. In a word, relative to the single component Pt, due to the boosting effects from the foreign Ni, Co, and Mn atoms, i.e., the well-designed reverse charge transfers and high-entropy configuration, the adsorption behaviors of oxygen-containing intermediates on the activated Pt sites are fundamentally tuned, which contributes to both the less energy-consuming processes of Li_2O_2 growth and decomposition.

Then, the adsorption behaviors of active sites concerning oxygen-containing intermediates further govern the free energy pathways during ORR and OER. As depicted in Figures 7b,c, S38 and S39, the calculated Gibbs free energy pathways with the four-electron process and optimized adsorption configurations on various intermediates ($O_2 \rightarrow LiO_2 \rightarrow Li_2O_2 \rightarrow Li_3O_4 \rightarrow Li_4O_4$) are shown for both Pt HEA and pure Pt NPs, respectively.[7,48−50] Gibbs free energy difference values facilitate the identification of the rate-determining step (RDS). For ORR, the RDS values for Pt HEA and pure Pt NPs are both identified as the reduction of Li_2O_2 to Li_3O_4, highlighted by the purple region. However, it is worthy of note that for OER, the RDS of Pt HEA is identified as the oxidation of LiO_2 to O_2 with a smaller energy barrier of 3.77 eV, whereas the RDS of Pt NPs is determined to be the oxidation of Li_4O_4 to Li_3O_4 (labeled by the green area) with an energy barrier of 3.82 eV. These variations indicate that relative to pure Pt NPs, Pt HEA demonstrates different electrochemical behaviors during the OER process, which helps reduce the Li_2O_2 decomposition energy barrier and enhance the Li_2O_2 conversion efficiency. Then the theoretical thermodynamic overpotentials are derived from the equations

$\eta_{ORR} = U_{eq} - U_{DC}$ and $\eta_{OER} = U_C - U_{eq}$, where U_{eq}, U_{DC}, and U_C represent the equilibrium, discharge, and charge voltages, respectively.[16,51] Although Pt HEA achieves a similar η_{ORR} value of 0.43 V, its η_{OER} value is reduced to 0.45 V compared with pure Pt NPs (0.66 V), indicating faster OER catalytic kinetics. Herein, the theoretically calculated overpotential values confirm that the optimized electronic structure and intermediate adsorption characteristic within Pt HEA promote the formation of a more favorable morphology of the Li_2O_2 products and fundamentally change the catalytic mechanism of the OER process, thus improving the utilizing efficiency of active sites and enhancing the overall catalytic performance.

Subsequent calculations of the partial density of states (PDOS) for Pt HEA and pure Pt NPs further illustrate their electronic structures, as shown in Figure 7d. It is revealed that the calculated *d*-band center of Pt HEA (−1.91 eV) shifts upward by 0.42 eV compared to that of Pt NPs (−2.33 eV). The upshift of the d-band center of Pt HEA to the Fermi energy level indicates that the electron localization stemmed from the intense interaction between Pt and Ni, Co, and Mn within Pt HEA. According to the consensus conclusion, due to the electron donation to adjacent Ni, Co, and Mn atoms, Pt demonstrates a feature of upshifted d-band center, which allows for the antibonding states of both the substrate and adsorbed intermediates to shift away from the Fermi level. This gives rise to the decreased antibonding state filling and contributes to a larger adsorbate adsorption strength, which is consistent with the strengthened affinity on the O_2 and LiO_2 of Pt HEA in Figure 7a. Herein, this reverse charge transfer between Pt and Ni, Co, and Mn makes Pt HEA@N−C quite suitable for regulating the growth behavior of Li_2O_2, laying a solid foundation for catalyzing the O_2 redox reaction of Li−O_2 batteries. Then, Figures 7e−h and S40 illustrate the charge density difference plots and Bader charge analysis of Pt HEA and Pt NPs with the O_2 and LiO_2 molecules adsorbed on the surfaces, respectively. The plots visually represent that effective charge transfer paths are established through metal−oxygen bonding, which leads to the redistribution of electrons from the catalyst substrate to the absorbed oxygen-containing species. It is noteworthy that both the calculated charge transfer numbers for O_2 (0.575) and LiO_2 (0.198) adsorbed on the Pt HEA surface are much larger than that of Pt NPs (0.459 and 0.031, respectively). This phenomenon indicates that Pt HEA has a more prominent affinity and accelerated electron transfer tendency for the intermediates, particularly for LiO_2, where the two O atoms are captured by the three neighboring metal sites on the Pt HEA surface, forming a more stable adsorption structure and a faster charge transfer channel. As a result, on the basis of the combined in-depth theoretical and experimental results, we infer that electron redistribution, which surmounts the electronegativity differences among the Pt, Ni, Co, and Mn atoms, governs the charge rearrangement in the region surrounding the active Pt. More importantly, the disordered high-entropy coordination environment further contributes to tuning the electronic structure of Pt. It can be concluded that these two critical factors are conducive to the regulation of thermodynamically favorable and reversible reaction pathways for Li_2O_2 formation/oxidation, which in turn benefit from reducing the reaction energy barrier and accelerating both the ORR and the OER conversion kinetics of Pt HEA@N−C. This endows Pt HEA@N−C with a much-ameliorated bifunctional catalysis performance when used for Li−O_2 batteries. The as-achieved ultralow potential and excellent cycling stability position it among the best in the reported Li−O_2 battery catalysts.

CONCLUSIONS

In summary, based on upcyling Ni, Co, and Mn valuable metals from spent $LiNi_{1/3}Mn_{1/3}Co_{1/3}O_2$ cathodes, we have first engineered a general and rapid synthesis strategy of ultrafine αNiCoMn (α = Pt, Ir, Ru) HEA NPs stabilized on nitrogen-doped carbon (N−C) frameworks, which demonstrate excellent bifunctional catalytic activity. As a proof-of-concept application in Li−O_2 batteries, the optimized Pt HEA@N−C catalyst harvests an unprecedented overall voltage gap of only 0.27 V and an excellent cycling performance exceeding 240 cycles. A series of atom-level HAADF-STEM, XANES, and FT-EXAFS results confirm that due to the high-energy transient shock contributed by Joule heating, there exists a desired structurally disordered high-entropy coordination environment within the whole HEA solid solution. More importantly, interesting reverse electron transfer occurs from higher electronegative Pt to surrounding Ni, Co, and Mn atoms. Experimental results together with DFT calculations disclose that this unconventional electron donation−acceptation orientation is advantageous for strengthening 5d−3d hybridization and triggering reduced electronic occupancy of the Pt antibonding states for Pt HEA@N−C. Meanwhile, its intrinsic high-entropy coordination environment further induces highly active catalysis surfaces by virtue of the cocktail effect. These promotions contribute to optimizing the d-electron structure, enhancing the adsorption strength and charge transfer efficiency toward the O_2-involved intermediates for Pt HEA@N−C. As expected, the Pt HEA@N−C catalyst manipulates the nucleation, growth, and oxidation behaviors of nanoscale Li_2O_2 products, realizing more energetically favorable ORR/OER and thus a reduced O_2 redox energy barrier, which are validated by a series of ex situ characterizations. Herein, our study not only advances the scope for the recycling of waste $LiNi_{1-x-y}Mn_xCo_yO_2$-based lithium-ion batteries into versatile electrocatalysis fields but also opens up an innovative avenue of catalytic activity activation via the fresh reverse charge transfer and high-entropy stabilization strategies.

EXPERIMENTAL METHODS

Preparation of N−C. First, sodium citrate and urea precursors were fully mixed and ground at a ratio of 10:1. Then, the powders were calcined within a tube furnace at 750 °C under a pure argon atmosphere for 1 h. The obtained black powders were filtered and washed using deionized water and anhydrous ethanol in turn 3 times and then were dried overnight to obtain the porous N−C substrate.

Preparation of the NCM Extract. The waste $LiNi_{1/3}Mn_{1/3}Co_{1/3}O_2$-type lithium-ion battery pack (nominal voltage of 3.6 V, nominal capacity of 100 Ah, open-circuit voltage of 3.97 V) from an electric vehicle was first discharged to a safe voltage. The remaining power in the waste battery could be depleted by connecting the battery in parallel with the resistor, and when the voltage of the waste battery was 1.0 V or less, it could be safely dismantled by hand within a fume hood. Then, the recycled $LiNi_{1/3}Mn_{1/3}Co_{1/3}O_2$ ternary cathode was soaked in the solution of *N*-methyl-2-pyrrolidone (NMP) to realize the sufficient dissolution of the poly(vinylidene fluoride) (PVDF) binder by virtue of ultrasonication for 12 h. During this process, the cathode material powders were absolutely stripped from the Al foil collector without the introduction of any impurities. Then, after 12 h of vacuum drying, black precursor powders could be obtained. 0.5 g of black powder was then dissolved in 1 M oxalic acid solution (40 mL). After fully stirring for 4 h at 90 °C, oxalate precipitates with the extraction of lithium ions were collected and dried to obtain black powders. After that, 0.5 g of black powder was dissolved in a 4 M nitric acid solution

(40 mL). After centrifugation 3 times, carbon black and other insoluble impurities were fully removed, while the recycled Ni, Co, and Mn ions were stabilized in the nitric acid liquid supernatant (NCM extract).

Preparation of Pt HEA@N−C, Pt@N−C, and NCM@N−C. Typically, 50 mg of N−C substrate, 4.13 mL of NCM extract, and 43.88 mg of $H_2PtCl_6·6H_2O$ were dispersed in 40 mL of anhydrous ethanol in turn, during which the molar ratio of Pt, Ni, Co, and Mn atoms was controlled as 1:1:1:1. After stirring at room temperature for 12 h, the precipitates were collected by centrifugation and then fully dried to get black powders. Subsequently, the precursor powder was heated by a Joule heating device with a rapid increase in temperature to 900 °C, followed by a very rapid cooling to room temperature, inducing the multielement mixing to yield the Pt HEA@N−C composite. For comparison, the Pt@N−C and NCM@N−C catalysts were also fabricated by the same procedure without the addition of the NCM extract and $H_2PtCl_6·6H_2O$, respectively.

Characterizations. The morphological features of the samples were thoroughly investigated using a field emission scanning electron microscope (Hitachi SU-8010) and TEM (Talos 200 S, FEI). HAADF-STEM analyses were conducted on an FEI Themis Z microscope equipped with a double Cs corrector operating at 300 kV. XRD patterns were obtained by analyzing the samples using an X-ray analyzer under Cu Kα radiation conditions. The valence states of the elements on the surface of the samples were recorded by XPS (Thermo Scientific Escalab 250Xi). Nitrogen adsorption and desorption isotherms and pore size distributions of the samples were obtained by using a Beishide 3H-2000 PS/PM system. XANES and EXAFS spectra were recorded at beamline BL14B2 of the SPring-8, Japan Synchrotron Radiation Research Institute, utilizing a pair of channel-cut Si (111) crystals for a monochromatic X-ray beam. The storage ring operated at 8.0 GeV with an average electron current of 99.5 mA. EXAFS data fitting was performed by using the Athena and Artemis programs from the Demeter data analysis package.

DFT Calculation. Spin-polarized density functional theory (DFT) calculations were performed using the Vienna ab initio simulation package (VASP), which utilizes plane-wave basis sets and projection-enhanced wave methods. The exchange-correlation potential was addressed through the generalized gradient approximation with Perdew−Burke−Ernzerhof parameters. The energy cutoff was set to 450 eV. A 2 × 2 × 1 Monkhorst−Pack grid centered around the gamma point was used for Brillouin-zone integration in VASPKIT7, with a Gaussian smearing width of 0.05 eV to allow for the partial occupation of Kohn−Sham orbitals. The structure was optimized to full relaxation, ensuring forces on each atom were below 0.03 eV/Å and energy convergence reached 10^{-5} eV. To accurately model molecular interactions with the material, van der Waals corrections were applied using Grimme's DFT-D3 method. To mitigate periodic boundary effects, a vacuum layer of 15 Å was added perpendicular to the interface. O_2 and LiO_2 molecules were placed in a 10 × 10 × 10 Å box and subjected to geometry optimization and self-consistent field calculations with a single Γ-point sampling. The adsorption energy (ΔE_{ads}) was employed to quantify the adsorption strength between components within a catalyst. This is achieved through the following calculation: $\Delta E_{ads} = E_{total} - E_{molecule} - E_{substrate}$. In this formula, E_{total} represents the total energy of the system, $E_{molecule}$ represents the energy of the isolated molecules, and $E_{substrate}$ represents the energy of the substrate material. The greater the absolute value of the ΔE_{ads}, the more pronounced the strength of adsorption between the system's components.

Catalyst Performance Tests. The synthesized catalyst (80 wt %), carbon (10 wt %, Timcal Super C65), and PVDF (10 wt %) were added to a vial and homogeneously dissolved in NMP prior to the preparation of the catalyst slurry. The slurries were then uniformly coated on carbon paper with a diameter of 14 mm. Then, the working cathode could be obtained after drying in a vacuum oven at 60 °C for 12 h with the active catalyst loading controlled at 0.4−0.5 mg cm^{-2}. 2032-coin cells were assembled in a glovebox under an Ar atmosphere ($O_2 \leq 0.1$ ppm, $H_2O \leq 0.1$ ppm), comprising a lithium anode, a glass fiber separator (GF/D), a cathode loaded with a catalyst, and 180 μL of electrolyte (1 M LiTFSI/TEGDME). Subsequently, the assembled cells were placed in a pure oxygen-filled airtight box and kept open-circuit for 10 h. The three catalyst-equipped $Li-O_2$ batteries were subjected to electrochemical testing using a program-controlled LANHE CT2001A battery test system. In addition, the CV tests were conducted using an electrochemical workstation (CHI760e) with a scan rate of 0.1 mV s^{-1} and a potential control of 2.0−4.5 V. EIS tests were also measured on the CHI760e electrochemical workstation with a frequency range of 10^{-2}−10^5 Hz and an amplitude of 5 mV. All of the tests were conducted at a room temperature of 25 ± 1 °C.

ASSOCIATED CONTENT

Supporting Information

The Supporting Information is available free of charge at https://pubs.acs.org/doi/10.1021/acsnano.5c00704.

> Detailed information about characterizations, such as XRD, TEM, XPS, BET, Raman, and EXAFS; detailed information about performances, such as CV, discharge−charge curves, EIS, and cycling stability; and DFT calculations (PDF)

AUTHOR INFORMATION

Corresponding Authors

Peng Wang − *College of Electromechanical Engineering, Shandong Engineering Laboratory for Preparation and Application of High-Performance Carbon-Materials, Qingdao University of Science & Technology, Qingdao 266061, PR China*; Email: pengwang@qust.edu.cn

Zhiming Liu − *College of Electromechanical Engineering, Shandong Engineering Laboratory for Preparation and Application of High-Performance Carbon-Materials, Qingdao University of Science & Technology, Qingdao 266061, PR China; Qingdao Industrial Energy Storage Research Institute, Qingdao Institute of Bioenergy and Bioprocess Technology, Chinese Academy of Sciences, Qingdao 266101, PR China*; orcid.org/0000-0001-8184-1116; Email: zmliu@qust.edu.cn

Authors

Shan Guo − *College of Electromechanical Engineering, Shandong Engineering Laboratory for Preparation and Application of High-Performance Carbon-Materials, Qingdao University of Science & Technology, Qingdao 266061, PR China*

Yongbin Xu − *College of Electromechanical Engineering, Shandong Engineering Laboratory for Preparation and Application of High-Performance Carbon-Materials, Qingdao University of Science & Technology, Qingdao 266061, PR China*

Xinyi Yuan − *College of Electromechanical Engineering, Shandong Engineering Laboratory for Preparation and Application of High-Performance Carbon-Materials, Qingdao University of Science & Technology, Qingdao 266061, PR China*

Yu Tian − *College of Electromechanical Engineering, Shandong Engineering Laboratory for Preparation and Application of High-Performance Carbon-Materials, Qingdao University of Science & Technology, Qingdao 266061, PR China*

Binchao Xu − *College of Electromechanical Engineering, Shandong Engineering Laboratory for Preparation and Application of High-Performance Carbon-Materials, Qingdao University of Science & Technology, Qingdao 266061, PR China*

Zhijun Zhao − *College of Electromechanical Engineering, Shandong Engineering Laboratory for Preparation and*

Application of High-Performance Carbon-Materials, Qingdao University of Science & Technology, Qingdao 266061, PR China

Yuxiao Wang − *College of Electromechanical Engineering, Shandong Engineering Laboratory for Preparation and Application of High-Performance Carbon-Materials, Qingdao University of Science & Technology, Qingdao 266061, PR China*

Jianwei Li − *College of Electromechanical Engineering, Shandong Engineering Laboratory for Preparation and Application of High-Performance Carbon-Materials, Qingdao University of Science & Technology, Qingdao 266061, PR China*

Xiaojun Wang − *College of Electromechanical Engineering, Shandong Engineering Laboratory for Preparation and Application of High-Performance Carbon-Materials, Qingdao University of Science & Technology, Qingdao 266061, PR China*

Complete contact information is available at:
https://pubs.acs.org/10.1021/acsnano.5c00704

Author Contributions

P.W., S.G., and Y.X.: Data curation. P.W., S.G., Y.X., and Y.T.: Formal analysis. P. W. and Z. L.: Funding acquisition. S.G., Y.X., X.Y., and Y.T.: Investigation. P.W., S.G., Y.X., B.X., and Z.Z.: Methodology. P.W. and Z.L.: Project administration. S.G., Y.X., and X.Y.: Resources. P.W. and Z.L.: Supervision. P.W., Y.W., J.L., and X.W.: Validation. P.W., S.G., Y.W., J.L., and X.W.: Visualization. P.W. and S.G.: Writing—original draft. P.W., S.G., and Z.L.: Writing—review and editing.

Notes

The authors declare no competing financial interest.

ACKNOWLEDGMENTS

This work was funded by the National Natural Science Foundation of China (Grant Nos. 21905152, 52302273), the Taishan Scholar Project of Shandong Province of China (Grant Nos. tsqn202211160 and tsqn202312199), the Youth Innovation Team Project for Talent Introduction and Cultivation in Universities of Shandong Province, the Shandong Provincial Natural Science Foundation of China (Grant No. ZR2023QE176), the Science and Technology Special Project of Qingdao City (24-1-8-cspz-12 nsh), and the China Postdoctoral Science Foundation (Grant No. 2022M713249).

REFERENCES

(1) Wang, P.; Ren, Y.; Wang, R.; Zhang, P.; Ding, M.; Li, C.; Zhao, D.; Qian, Z.; Zhang, Z.; Zhang, L.; Yin, L. Atomically Dispersed Cobalt Catalyst Anchored on Nitrogen-Doped Carbon Nanosheets for Lithium-Oxygen Batteries. *Nat. Commun.* **2020**, *11* (1), 1576.

(2) Kang, J.-H.; Lee, J.; Jung, J.-W.; Park, J.; Jang, T.; Kim, H.-S.; Nam, J.-S.; Lim, H.; Yoon, K. R.; Ryu, W.-H.; Kim, I.-D.; Byon, H. R. Lithium−Air Batteries: Air-Breathing Challenges and Perspective. *ACS Nano* **2020**, *14* (11), 14549−14578.

(3) Liu, T.; Vivek, J. P.; Zhao, E. W.; Lei, J.; Garcia-Araez, N.; Grey, C. P. Current Challenges and Routes Forward for Nonaqueous Lithium-Air Batteries. *Chem. Rev.* **2020**, *120* (14), 6558−6625.

(4) Wang, P.; Zhao, D.; Zhang, P.; Hui, X.; Zhang, Z.; Wang, R.; Wang, C.; Ge, X.; Liu, X.; Li, Y.; Yin, L. P-Block Element Modulated 1 T Phase MoS_2 with Ru Lattice Grafting for High-Performance Li∥O_2 Batteries. *Nat. Commun.* **2025**, *16* (1), 1453.

(5) Sun, Z.; Lin, X.; Wang, C.; Tan, Y.; Dou, W.; Hu, A.; Cui, J.; Fan, J.; Yuan, R.; Zheng, M.; Dong, Q. Constructing an Interlaced Catalytic Surface via Fluorine-Doped Bimetallic Oxides for Oxygen Electrode Processes in Li-O_2 Batteries. *Adv. Mater.* **2024**, *36* (31), No. 2404319.

(6) Zhou, Y.; Gu, Q.; Xin, Y.; Tang, X.; Wu, H.; Guo, S. Orbital Coupling of PbO_7 Node in Single-Crystal Metal-Organic Framework Enhances Li-O_2 Battery Electrocatalysis. *Nano Lett.* **2023**, *23* (22), 10600−10607.

(7) Guo, Y.; Wang, P.; Liu, Y.; Guo, S.; Shi, L.; Sun, J.; Tian, Y.; Wang, X.; Zhao, S.; Liu, Z. Dual-Type Atomic Ru Promoted Bifunctional Catalytic Process Realizing Ultralow Overpotential for Li-O_2 Batteries. *Appl. Catal., B* **2024**, *356*, No. 124203.

(8) Bai, T.; Li, D.; Xiao, S.; Ji, F.; Zhang, S.; Wang, C.; Lu, J.; Gao, Q.; Ci, L. Recent Progress on Single-Atom Catalysts for Lithium-Air Battery Applications. *Energy Environ. Sci.* **2023**, *16* (4), 1431−1465.

(9) Zhang, K.; Liu, H.; Qu, S.; Cao, W.; Zhang, J.; Cao, D.; Wang, J.; Song, T.; Shao, R.; Li, X.; Wu, F.; Tan, G. Integrated Platinum-Fullerene Nanocatalyst as Efficient Cathode Kinetic Promoter for Advanced Lithium-oxygen Batteries. *Energy Storage Mater.* **2024**, *69*, No. 103428.

(10) Jung, W.-B.; Park, H.; Jang, J.-S.; Kim, D. Y.; Kim, D. W.; Lim, E.; Kim, J. Y.; Choi, S.; Suk, J.; Kang, Y.; Kim, I.-D.; Kim, J.; Wu, M.; Jung, H.-T. Polyelemental Nanoparticles as Catalysts for a Li-O_2 Battery. *ACS Nano* **2021**, *15* (3), 4235−4244.

(11) Li, Y.; Li, Y.; Ding, Y.; Ma, J.; Das, P.; Zhang, B.; Wu, Z.-S.; Bao, X. Spatially Confined Sub-Nanometer Pt in RuO_2 Nanosheet as Robust Bifunctional Oxygen Electrocatalyst for Stabilizing Li-O_2 Batteries. *Chem. Catal.* **2023**, *3* (9), No. 100658.

(12) Rao, Y.; Yang, J.; Tian, J.; Ning, W.; Guo, S.; Zhou, H. The Spin-Selective Channels in Fully-Exposed PtFe Clusters Enable Fast Cathodic Kinetics of Li-O_2 Battery. *Angew. Chem., Int. Ed.* **2025**, *64* (7), No. e202418893.

(13) Zhang, E.; Dong, A.; Yin, K.; Ye, C.; Zhou, Y.; Tan, C.; Li, M.; Zheng, X.; Wang, Y.; Gao, X.; Li, H.; Wang, D.; Guo, S. Electron Localization in Rationally Designed Pt_1Pd Single-Atom Alloy Catalyst Enables High-Performance Li-O_2 Batteries. *J. Am. Chem. Soc.* **2024**, *146* (4), 2339−2344.

(14) Liu, Y.; Liu, G.; Chen, X.; Xue, C.; Sun, M.; Liu, Y.; Kang, J.; Sun, X.; Guo, L. Achieving Negatively Charged Pt Single Atoms on Amorphous $Ni(OH)_2$ Nanosheets with Promoted Hydrogen Absorption in Hydrogen Evolution. *Nano-Micro Lett.* **2024**, *16* (1), 202.

(15) Wu, R.; Meng, Q.; Yan, J.; Zhang, Z.; Chen, B.; Liu, H.; Tai, J.; Zhang, G.; Zheng, L.; Zhang, J.; Han, B. Intermetallic Synergy in Platinum-Cobalt Electrocatalysts for Selective C-O Bond Cleavage. *Nat. Catal.* **2024**, *7* (6), 702−718.

(16) Zhang, P.; Hui, X.; Nie, Y.; Wang, R.; Wang, C.; Zhang, Z.; Yin, L. New Conceptual Catalyst on Spatial High-Entropy Alloy Heterostructures for High-Performance Li-O_2 Batteries. *Small* **2023**, *19* (15), No. 2206742.

(17) Xiao, Y.; Ying, J.; Chen, J.; Yang, X.; Tian, G.; Li, J.; Janiak, C.; Yang, X. Phosphorous Incorporated PtNi Networks with Synergistic Directional Electron Transfer for Efficient and Durable Seawater Hydrogen Production. *Adv. Funct. Mater.* **2024**, *35* (15), No. 2418264.

(18) Zhou, Y.; Gu, Q.; Yin, K.; Li, Y.; Tao, L.; Tan, H.; Yang, Y.; Guo, S. Engineering eg Orbital Occupancy of Pt with Au Alloying Enables Reversible Li-O_2 Batteries. *Angew. Chem., Int. Ed.* **2022**, *61* (26), No. e202201416.

(19) Hao, J.; Zhuang, Z.; Cao, K.; Gao, G.; Wang, C.; Lai, F.; Lu, S.; Ma, P.; Dong, W.; Liu, T.; Du, M.; Zhu, H. Unraveling the Electronegativity-Dominated Intermediate Adsorption on High-Entropy Alloy Electrocatalysts. *Nat. Commun.* **2022**, *13* (1), 2662.

(20) Shi, W.; Liu, H.; Li, Z.; Li, C.; Zhou, J.; Yuan, Y.; Jiang, F.; Fu, K. K.; Yao, Y. High-entropy Alloy Stabilized and Activated Pt Clusters for Highly Efficient Electrocatalysis. *SusMat* **2022**, *2* (2), 186−196.

(21) Liang, J.; Cao, G.; Zeng, M.; Fu, L. Controllable Synthesis of High-Entropy Alloys. *Chem. Soc. Rev.* **2024**, *53* (12), 6021−6041.

(22) Feng, G.; Ning, F.; Song, J.; Shang, H.; Zhang, K.; Ding, Z.; Gao, P.; Chu, W.; Xia, D. Sub-2 Nm Ultrasmall High-Entropy Alloy Nanoparticles for Extremely Superior Electrocatalytic Hydrogen Evolution. *J. Am. Chem. Soc.* **2021**, *143* (41), 17117−17127.

(23) Yao, Y.; Dong, Q.; Brozena, A.; Luo, J.; Miao, J.; Chi, M.; Wang, C.; Kevrekidis, I. G.; Ren, Z. J.; Greeley, J.; Wang, G.; Anapolsky, A.; Hu, L. High-Entropy Nanoparticles: Synthesis-Structure-Property Relationships and Data-Driven Discovery. *Science* **2022**, *376* (6589), No. eabn3103.

(24) Zhou, Y.; Shen, X.; Wang, M.; Zhang, L.; Qian, T.; Yan, C.; Lu, J. The Understanding, Rational Design, and Application of High-Entropy Alloys as Excellent Electrocatalysts: A Review. *Sci. China Mater.* **2023**, *66* (7), 2527−2544.

(25) Liu, S.; Shen, Y.; Zhang, Y.; Cui, B.; Xi, S.; Zhang, J.; Xu, L.; Zhu, S.; Chen, Y.; Deng, Y.; Hu, W. Extreme Environmental Thermal Shock Induced Dislocation-Rich Pt Nanoparticles Boosting Hydrogen Evolution Reaction. *Adv. Mater.* **2022**, *34* (2), No. 2106973.

(26) Hao, J.; Zhuang, Z.; Hao, J.; Cao, K.; Hu, Y.; Wu, W.; Lu, S.; Wang, C.; Zhang, N.; Wang, D.; Du, M.; Zhu, H. Strain Relaxation in Metal Alloy Catalysts Steers the Product Selectivity of Electrocatalytic CO_2 Reduction. *ACS Nano* **2022**, *16* (2), 3251−3263.

(27) Liu, S.; Hu, Z.; Wu, Y.; Zhang, J.; Zhang, Y.; Cui, B.; Liu, C.; Hu, S.; Zhao, N.; Han, X.; Cao, A.; Chen, Y.; Deng, Y.; Hu, W. Dislocation-Strained IrNi Alloy Nanoparticles Driven by Thermal Shock for the Hydrogen Evolution Reaction. *Adv. Mater.* **2020**, *32* (48), No. 2006034.

(28) Wang, Y.; Li, Z.; Zheng, X.; Wu, R.; Song, J.; Chen, Y.; Cao, X.; Wang, Y.; Nie, Y. Renovating Phase Constitution and Construction of Pt Nanocubes for Electrocatalysis of Methanol Oxidation via a Solvothermal-Induced Strong Metal-Support Interaction. *Appl. Catal., B* **2023**, *325*, No. 122383.

(29) Jin, H.; Xu, Z.; Hu, Z.-Y.; Yin, Z.; Wang, Z.; Deng, Z.; Wei, P.; Feng, S.; Dong, S.; Liu, J.; Luo, S.; Qiu, Z.; Zhou, L.; Mai, L.; Su, B.-L.; Zhao, D.; Liu, Y. Mesoporous Pt@Pt-Skin Pt_3Ni Core-Shell Framework Nanowire Electrocatalyst for Efficient Oxygen Reduction. *Nat. Commun.* **2023**, *14* (1), 1518.

(30) You, Y.; Han, P.; Song, S.; Luo, W.; Zhao, S.; Han, K.; Tian, Y.; Yan, N.; Li, X. Distinct Selectivity Control in Solar-Driven Bio-Based α-Hydroxyl Acid Conversion: A Comparison of Pt Nanoparticles and Atomically Dispersed Pt on CdS. *Angew. Chem., Int. Ed.* **2023**, *62* (43), No. e202306452.

(31) Wang, C.; Zhang, J.; Miao, K.; Long, M.; Lai, S.; Zhao, S.; Kang, X. Octahedral Nanocrystals of Ru-Doped PtFeNiCuW/CNTs High-Entropy Alloy: High Performance Toward pH-Universal Hydrogen Evolution Reaction. *Adv. Mater.* **2024**, *36* (33), No. 2400433.

(32) Zhang, Y.; Zhao, Q.; Danil, B.; Xiao, W.; Yang, X. Oxygen-Vacancy-Induced Formation of Pt-Based Intermetallics on MXene with Strong Metal-Support Interactions for Efficient Oxygen Reduction Reaction. *Adv. Mater.* **2024**, *36* (25), No. 2400198.

(33) Yin, S.; Yan, Y.-N.; Chen, L.; Cheng, N.; Cheng, X.; Huang, R.; Huang, H.; Zhang, B.; Jiang, Y.-X.; Sun, S.-G. FeN4 Active Sites Electronically Coupled with PtFe Alloys for Ultralow Pt Loading Hybrid Electrocatalysts in Proton Exchange Membrane Fuel Cells. *ACS Nano* **2024**, *18* (1), 551−559.

(34) Yang, Q.; Liu, H.; Yuan, P.; Jia, Y.; Zhuang, L.; Zhang, H.; Yan, X.; Liu, G.; Zhao, Y.; Liu, J.; Wei, S.; Song, L.; Wu, Q.; Ge, B.; Zhang, L.; Wang, K.; Wang, X.; Chang, C.-R.; Yao, X. Single Carbon Vacancy Traps Atomic Platinum for Hydrogen Evolution Catalysis. *J. Am. Chem. Soc.* **2022**, *144* (5), 2171−2178.

(35) Zhu, J.; Xia, L.; Yu, R.; Lu, R.; Li, J.; He, R.; Wu, Y.; Zhang, W.; Hong, X.; Chen, W.; Zhao, Y.; Zhou, L.; Mai, L.; Wang, Z. Ultrahigh Stable Methanol Oxidation Enabled by a High Hydroxyl Concentration on Pt Clusters/MXene Interfaces. *J. Am. Chem. Soc.* **2022**, *144* (34), 15529−15538.

(36) Cai, B.; Shen, D.; Xie, Y.; Yan, H.; Wang, Y.; Chen, X.; Wang, L.; Fu, H. Unlocking Superior Hydrogen Oxidation and CO Poisoning Resistance on Pt Enabled by Tungsten Nitride-Mediated Electronic Modulation. *J. Am. Chem. Soc.* **2024**, *146* (48), 33193−33203.

(37) Palani, R.; Wu, Y.-S.; Wu, S.-H.; Chien, W.-C.; Lue, S. J.; Jose, R.; Yang, C.-C. Fascinating Bifunctional Electrocatalytic Activity via a Mesoporous Structured $FeMnO_3$@ZrO_2 Matrix as an Efficient Cathode for Li-O_2 Batteries. *ACS Appl. Energy Mater.* **2023**, *6* (9), 4734−4747.

(38) Kim, C.; Sul, J.; Moon, J. H. Semiconductor Process Fabrication of Multiscale Porous Carbon Thin Films for Energy Storage Devices. *Energy Storage Mater.* **2023**, *57*, 308−315.

(39) Li, D.; Zhao, L.; Wang, J.; Yang, C. Tailoring the d-Band Center over Isomorphism Pyrite Catalyst for Optimized Intrinsic Affinity to Intermediates in Lithium-Oxygen Batteries. *Adv. Energy Mater.* **2023**, *13* (15), No. 2204057.

(40) Zhang, Y.; Zhang, S.; Ma, J.; Chen, X.; Nan, C.; Chen, C. Single-Atom-Mediated Spinel Octahedral Structures for Elevated Performances of Li-Oxygen Batteries. *Angew. Chem., Int. Ed.* **2023**, *62* (15), No. e202218926.

(41) Lv, Q.; Zhu, Z.; Ni, Y.; Wen, B.; Jiang, Z.; Fang, H.; Li, F. Atomic Ruthenium-Riveted Metal−Organic Framework with Tunable d-Band Modulates Oxygen Redox for Lithium-Oxygen Batteries. *J. Am. Chem. Soc.* **2022**, *144* (50), 23239−23246.

(42) Park, M.; Cho, S.; Yang, J.; Lau, V. W.; Kim, K. H.; Park, J. H.; Ringe, S.; Kang, Y.-M. Heterogeneous Catalyst as a Functional Substrate Governing the Shape of Electrochemical Precipitates in Oxygen-Fueled Rechargeable Batteries. *J. Am. Chem. Soc.* **2023**, *145* (28), 15425−15434.

(43) Zhang, Y.; Zhang, S.; Li, H.; Lin, Y.; Yuan, M.; Nan, C.; Chen, C. Tunable Oxygen Vacancies of Cobalt Oxides in Lithium−Oxygen Batteries: Morphology Control of Discharge Product. *Nano Lett.* **2023**, *23* (19), 9119−9125.

(44) Ke, S.-W.; Li, W.; Gu, Y.; Su, J.; Liu, Y.; Yuan, S.; Zuo, J.-L.; Ma, J.; He, P. Covalent Organic Frameworks with Ni-Bis(Dithiolene) and Co-Porphyrin Units as Bifunctional Catalysts for Li-O_2 Batteries. *Sci. Adv.* **2023**, *9* (5), No. eadf2398.

(45) Lian, Z.; Lu, Y.; Zhao, S.; Li, Z.; Liu, Q. Engineering the Electronic Interaction between Atomically Dispersed Fe and RuO_2 Attaining High Catalytic Activity and Durability Catalyst for Li-O_2 Battery. *Adv. Sci.* **2023**, *10* (9), No. 2205975.

(46) Wang, P.; Zhao, D.; Hui, X.; Qian, Z.; Zhang, P.; Ren, Y.; Lin, Y.; Zhang, Z.; Yin, L. Bifunctional Catalytic Activity Guided by Rich Crystal Defects in Ti_3C_2 MXene Quantum Dot Clusters for Li-O_2 Batteries. *Adv. Energy Mater.* **2021**, *11* (32), No. 2003069.

(47) Subhakumari, A.; Thomas, T.; Aetukuri, N. P. B. Parasitic Products Formed during Discharge Limit Capacity and Rechargeability in Li-O_2 Cells. *ACS Energy Lett.* **2024**, *9* (12), 6109−6116.

(48) Zhang, G.; Li, G.; Wang, J.; Tong, H.; Wang, J.; Du, Y.; Sun, S.; Dang, F. 2D SnSe Cathode Catalyst Featuring an Efficient Facet-Dependent Selective Li_2O_2 Growth/Decomposition for Li-Oxygen Batteries. *Adv. Energy Mater.* **2022**, *12* (21), No. 2103910.

(49) Tian, G.; Xu, H.; Wang, X.; Wen, X.; Liu, P.; Liu, S.; Zeng, T.; Fan, F.; Wang, S.; Wang, C.; Zeng, C.; Shu, C. Controllable Regulation of the Oxygen Redox Process in Lithium-Oxygen Batteries by High-Configuration-Entropy Spinel with an Asymmetric Octahedral Structure. *ACS Nano* **2024**, *18* (18), 11849−11862.

(50) Kondori, A.; Jiang, Z.; Esmaeilirad, M.; Tamadoni Saray, M.; Kakekhani, A.; Kucuk, K.; Navarro Munoz Delgado, P.; Maghsoudipour, S.; Hayes, J.; Johnson, C. S.; Segre, C. U.; Shahbazian-Yassar, R.; Rappe, A. M.; Asadi, M. Kinetically Stable Oxide Overlayers on Mo_3P Nanoparticles Enabling Lithium-Air Batteries with Low Overpotentials and Long Cycle Life. *Adv. Mater.* **2020**, *32* (50), No. 2004028.

(51) Zhao, C.; Yan, Z.; Zhou, B.; Pan, Y.; Hu, A.; He, M.; Liu, J.; Long, J. Identifying the Role of Lewis-base Sites for the Chemistry in Lithium-Oxygen Batteries. *Angew. Chem., Int. Ed.* **2023**, *62* (32), No. e202302746.